Geochemistry Geophysics Geosystems G3

Article
Volume 14, Number 9
3 September 2013
doi: 10.1002/ggge.20214
ISSN: 1525-2027

Published by AGU and the Geochemical Society

Overriding plate structure of the Nicaragua convergent margin: Relationship to the seismogenic zone of the 1992 tsunami earthquake

Valentí Sallarès, Adrià Meléndez, and Manuel Prada
Barcelona Center for Subsurface Imaging, Institute of Marine Sciences, Consejo Superior de Investigaciones Científicas, Barcelona, Spain (vsallares@icm.csic.es)

César R. Ranero
Barcelona Center for Subsurface Imaging, Institute of Marine Sciences, Consejo Superior de Investigaciones Científicas, Barcelona, Spain

Kirk McIntosh
Institute for Geophysics, University of Texas at Austin, Austin, Texas, USA

Ingo Grevemeyer
GEOMAR Helmholtz Centre for Marine Research, Kiel, Germany

[1] We present 2-D seismic velocity models and coincident multichannel seismic reflection images of the overriding plate and the inter-plate boundary of the Nicaragua convergent margin along two wide-angle seismic profiles parallel and normal to the trench acquired in the rupture area of the 1992 tsunami earthquake. The trench-perpendicular profile runs over a seamount subducting under the margin slope, at the location where seismological observations predict large coseismic slip. Along this profile, the igneous basement shows increasing velocity both with depth and away from the trench, reflecting a progressive decrease in upper-plate rock degree of fracturing. Upper mantle-like velocities are obtained at ~10 km depth beneath the fore-arc Sandino basin, indicating a shallow mantle wedge. A mismatch of the inter-plate reflector in the velocity models and along coincident multichannel seismic profiles under the slope is best explained by ~15% velocity anisotropy, probably caused by subvertical open fractures that may be related to fluid paths feeding known seafloor seepage sites. The presence of a shallow, partially serpentinized mantle wedge, and the fracture-related anisotropy are supported by gravity analysis of velocity-derived density models. The downdip limit of inter-plate seismicity occurs near the tip of the inferred mantle wedge, suggesting that seismicity could be controlled by the presence of serpentinite group minerals at the fault gouge. Near the trench, the inferred local increase of normal stress produced by the subducting seamount in the plate boundary may have made this fault segment unstable during earthquake rupture, which could explain its tsunamigenic character.

Components: 16,632 words, 11 figures.

Keywords: convergent margin; tsunami earthquake; wide-angle seismics; travel time tomography.

Index Terms: 0935 Seismic methods: Exploration Geophysics; 0915 Downhole methods: Exploration Geophysics; 7240 Subduction zones: Seismology; 7294 Seismic instruments and networks: Seismology; 7230 Seismicity and tectonics: Seismology; 1207 Transient deformation: Geodesy and Gravity; 1217 Time variable gravity: Geodesy and Gravity; 1219 Gravity anomalies and Earth structure: Geodesy and Gravity; 1240 Satellite geodesy: results: Geodesy and Gravity; 1242 Seismic cycle related deformations: Geodesy and Gravity; 3060 Subduction zone processes: Marine Geology and Geophysics; 3025 Marine seismics: Marine Geology and Geophysics; 1031 Subduction zone processes: Geochemistry; 3613 Sub-

© 2013. American Geophysical Union. All Rights Reserved.

duction zone processes: Mineralogy and Petrology; 8170 Subduction zone processes: Tectonophysics; 8413 Subduction zone processes: Volcanology.

Received 15 April 2013; **Revised** 25 June 2013; **Accepted** 25 June 2013; **Published** 3 September 2013.

Sallarès, V., A. Meléndez, M. Prada, C. R. Ranero, K. McIntosh, and I. Grevemeyer (2013), Overriding plate structure of the Nicaragua convergent margin: Relationship to the seismogenic zone of the 1992 tsunami earthquake, *Geochem. Geophys. Geosyst.*, *14*, 3436–3461, doi:10.1002/ggge.20214.

1. Introduction

[2] Most of the world's largest earthquakes are thrust events that occur along the plate interface between the underthrusting and overriding plates in subduction zones. These events nucleate within the so-called seismogenic zone [*Hyndman and Wang*, 1993; *Hyndman et al*., 1997], a region where the plates are mechanically coupled in some important degree and suddenly, episodically slip. The interpretation of the seismogenic zone is dependent on the data available for a particular region, and in this study, given the lack of geodetic data offshore, we assume that the location is roughly constrained by inter-plate seismicity recorded by different networks in the area. The updip and downdip limits of the seismogenic zone are inferred to reflect the frictional behavior at the fault gouge, which is generally accepted to involve a transition from stable, velocity-strengthening (i.e., aseismic) behavior of the minerals, outside the seismogenic zone, to unstable, velocity-weakening (i.e., seismogenic) behavior [e.g., *Marone and Saffer*, 2007]. In the case of the updip limit this transition has been attributed to a suite of physical transformations of material at the plate boundary and changes in the fluid abundance [e.g., *Moore and Vrolijk*, 1992; *Moore and Saffer*, 2001; *von Huene et al*., 2004; *Bangs et al*., 2004; *Ranero et al*., 2008]. In a number of cases the downdip limit occurs at the intersection of the inter-plate boundary with the continental Moho, and has been associated to the presence of velocity-strengthening hydrous minerals of the serpentinite group at the fault interface [e.g., *Peacock and Hyndman*, 1999; *Hyndman and Peacock*, 2003]. The location of the seismogenic zone limits along the plate interface is believed to depend on the thermal structure [*Tichelaar and Ruff*, 1993; *Oleskevich et al*., 1999] and the local stress field [*Scholz*, 1998], which are in turn controlled by a number of factors including the age of the subducting slab, the convergence rate, relief of the incoming plate, and the composition, structure and elastic properties of the overriding and incoming plates among others [e.g., *Ruff and Kanamori*, 1983; *Pacheco et al*., 1993; *Scholz and Campos*, 1995]. Some controlling factors, such as the age of the plate or the convergence rate, can be estimated from available regional data and models; but other ones, such as the geometry of the inter-plate boundary, or the physical properties and structure of the overriding and subducting plates and plates interface, can only be determined with specifically designed geophysical experiments.

[3] If the rupture of a thrust earthquake propagates updip to shallow levels, the displacement of the seafloor may generate a tsunami. Large earthquakes of magnitude above $M_w \sim 8$ are generally required to excite significant tsunamis [e.g., *Ward*, 1980]. However, there is a particular class of events called "tsunami earthquakes" that generate anomalously large tsunamis for their size [*Kanamori*, 1972]. One of the best documented tsunami earthquakes occurred on 2 September 1992, offshore Nicaragua (Figure 1). Despite its modest size ($M_s = 7.2$), this event excited a tsunami with run-up heights of up to ~10 m, killing 170 people and leaving over 13,000 homeless [*Baptista et al*., 1993; *Satake et al*., 1993]. The duration of the seismic event was exceptionally long for its size, meaning that the seismic rupture propagated at anomalously low speed [*Kikuchi and Kanamori*, 1995; *Satake*, 1995; *Ihmlé*, 1996a]. To explain the characteristics of this, and other, tsunami earthquakes, it has been proposed that the coseismic rupture should involve unusually shallow and weak segments along the plate interface [e.g., *Kanamori*, 1972; *Okal*, 1988; *Pelayo and Wiens*, 1992; *Kanamori and Kikuchi*, 1993; *Polet and Kanamori*, 2000] and local asperities such as subducting seamounts [*McIntosh et al*., 2007].

[4] In this work, we present 2-D seismic velocity and inter-plate geometry models obtained along two perpendicular refraction and wide-angle reflection seismic (WAS) profiles and coincident multichannel seismic reflection (MCS) images acquired over the rupture area of the 1992 earthquake (Figure 1). We

present evidence that supports that the structure and elastic properties of the upper-plate basement, together with the relief of the inter-plate boundary, have exerted a control to (1) determine the location of the limits of the inter-plate seismicity (i.e., the seismogenic zone), and (2) help to explain the rupture characteristics of the 1992 earthquake, that are anomalous because it ruptured shallower than the presumed updip limit of the seismogenic zone. We also show that the combination of WAS and MCS data, with the help of gravity modeling, allow to determine the upper-plate physical properties and inter-plate geometry at the resolution required to evaluate working hypotheses on the mechanical behavior of inter-plate fault zones.

[5] The paper is structured in five sections following this introduction. In section 2, we summarize the regional tectonic setting, in section 3, we present the data and methods, and in section 4, we describe the modeling results and model parameters uncertainty. In section 5, we discuss the implications concerning the nature and characteristics of the overriding plate and we argue the possible influence of the upper-plate structure and properties to control the location of the inter-plate seismogenic zone, as well as its potential role on the occurrence of the 1992 tsunami earthquake.

2. Tectonic Setting

[6] The Nicaraguan convergent margin is part of the Middle American Trench (MAT), where the oceanic Cocos plate subducts under the Central America portion of the Caribbean plate (Figure 1). The Cocos plate is moving toward the NE at a velocity of 91 mm/yr with respect to the Caribbean plate [*DeMets et al*., 1994] and the oceanic plate segment that is currently entering the trench axis is ~25 Myr old [*Barkhausen et al*., 2001]. The Cocos plate is increasingly faulted from the outer rise to the trench axis, with fault scarps of 100–500 m vertical offset, giving a stair-like pattern to the seafloor and forming half grabens that may expose basement

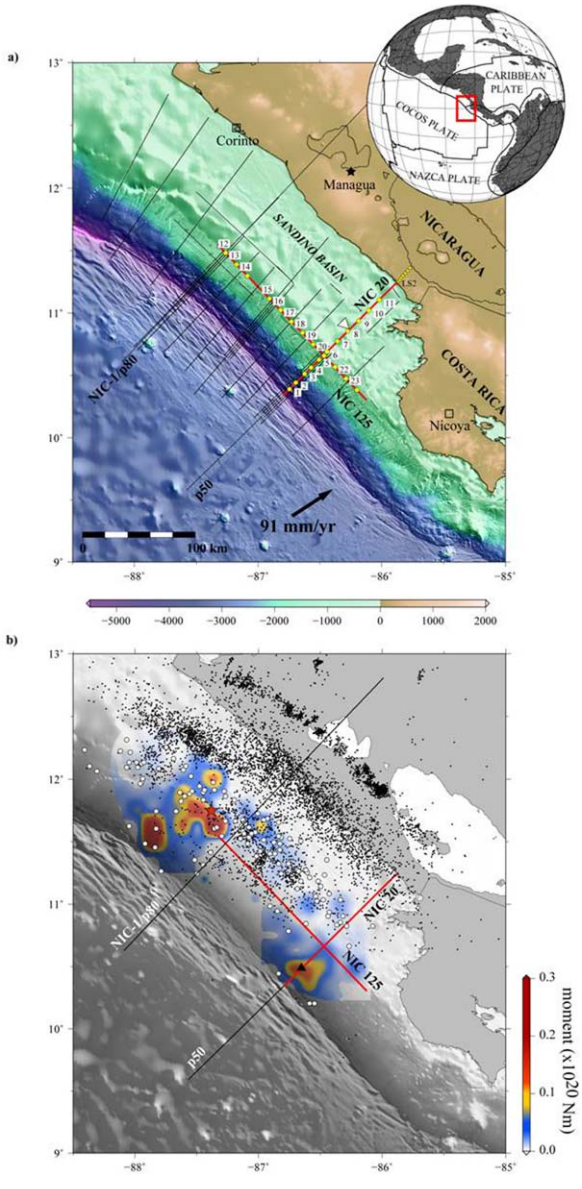

Figure 1. (a) Relief map of the study area off- and on-shore Nicaragua. Black lines show location of seismic profiles (MCS and WAS) acquired with R/V Maurice Ewing cruise EW00–05 in 2000. Red thick lines labeled NIC-20 and NIC-125 correspond to the WAS and MCS profiles discussed in this paper. Yellow circles and yellow triangles display OBHs and land stations deployed along these two profiles, respectively. Thick arrow correspond to the plate motion vector estimated using poles of Nuvel-1A [*DeMets et al*., 1994]. Inset: Regional tectonic map with tectonic plates and their boundaries. The red box encompasses the study area. Profile p50 marks the seaward extension of profile NIC-20 collected in a different cruise and presented by *Ivandic et al*. [2008], and p80 indicates the location of the WAS profile modeled by *Walther et al*. [2000], and MCS transect in *Ranero et al*. [2000].(b) Shaded bathymetry map of the study region overlaid by the map of inverted moment release of the 2 September 1992, tsunami earthquake that encompasses the source region [*Ihmlé*, 1996b]. Red star marks the epicentral location of the 1992 event, whereas white circles correspond to aftershocks within 3 months after the main shock [*Ihmlé*, 1996a]. Black dots are earthquakes recorded by the Nicaraguan seismic network onshore between 1975 and 1982. Solid lines correspond to the WAS profiles in Figure 1a. Black triangle indicates location of a subducted seamount imaged in MCS profiles.

[*Ranero et al*., 2000]. These normal faults were created at the spreading axis but are reactivated by plate bending trenchward of the outer rise.

[7] The MAT and Central America margin have been studied in greater extent offshore Guatemala and Costa Rica (for a comprehensive review, see Ranero et al. [2007]). The Guatemala segment was studied mainly during the 60–80s using geophysical data, including active seismics and potential-field methods [*Fisher*, 1961; *Seely et al*., 1974], and drilling done during Deep Sea Drilling Project (DSDP) Legs 67 and 84 [*von Huene et al*., 1985]. Initial interpretations described a large accretionary prism building the continental Guatemala margin [*Seely et al*., 1974], but later results showed the presence of a Mesozoic igneous basement without net accretion [*von Huene et al*., 1985]. The Costa Rica margin was first proposed to consist mainly of ophiolitic rocks similar to the Nicoya peninsula units [*Bourgeois et al*., 1984], later proposed to be accretionary [e.g., *Stoffa et al*., 1991; *McIntosh et al*., 1993], and subsequently nonaccretionary [*Hinz et al*., 1996; *Ye et al*., 1996; *Kimura et al*., 1997; *Barkhausen et al*., 2001; *Sallarès et al*., 1999, 2000]. More recently it has been proposed to be dominated by subduction erosion [e.g., *Ranero and von Huene*, 2000; *von Huene et al*., 2000; *Vannuchi et al*., 2003]. Further studies indicate that Guatemala has also undergone long-term large-scale subsidence that indicates continuous subduction erosion [*Vannuchi et al*., 2004].

[8] The Nicaragua margin, between Guatemala and Costa Rica, had been comparatively little explored until the mid 90s. The only early published data were from a single MCS profile (NIC-1) acquired by the University of Texas in the late 70s and first interpreted to show a well-developed accretionary prism [*Crowe and Buffler*, 1985]. However, later reprocessing of NIC-1 together with industry seismic data and exploration drill holes at the Sandino fore-arc basin under the shelf, and a coincident WAS profile collected in 1996 during Sonne cruise 107, allowed to demonstrate the lack of a large accretionary prism and the similarity of the basement to those in Guatemala and Costa Rica and imaged the inter-plate geometry down to the mantle wedge [*Walther et al*., 2000]. These data were also used to define the history of margin development and to propose that the Nicaragua margin has been affected by long-term tectonic erosion [*Ranero et al*., 2000]. The stratigraphic history of the fore-arc basin suggest that the basin originated in the Late Cretaceous (~75 Ma), coeval with the subduction initiation of the Farallon plate beneath the Caribbean plate.

3. Seismic Data Set and Modeling Strategy

3.1. Data Set

[9] The WAS data used in this study, which cover the rupture area of the 1992 tsunami earthquake, were recorded in 2000 during US R/V Maurice Ewing cruise EW00–05 (Figure 1). The experiment was designed to study the impact of subducting plate heterogeneities on the overriding plate structure and evolution, and their potential effects on inter-plate seismogenesis [*McIntosh et al*., 2007]. The experiment collected collocated MCS and WAS data along two onshore-offshore trench-perpendicular transects, and a third transect along the strike of the middle-upper slope. In this work we concentrate on the two WAS transects displayed in red in Figure 1. The WAS profiles have been modeled using forward modeling techniques in an unpublished PhD work [*Berhorst*, 2006], here we present the tomographic inversion of the data.

[10] The trench-perpendicular WAS line NIC-20 is ~160 km long and includes 11 GEOMAR Ocean Bottom Hydrophones (OBH) deployed from trench to the shelf, and 7 PASSCAL, Reftek land stations extending from the coastline to the volcanic arc. The ~190 km long trench-parallel profile NIC-125 was recorded on 12 OBH, and crosses NIC-20 at 52 km from the trench axis (Figure 1). The seismic source for the WAS profile was an airgun array with a total volume of 136 L shot every 60 s, with an average shot spacing of ~125 m. The quality of the WAS data is excellent concerning both amplitude and lateral coherency of seismic phases. Processing of WAS record consisted of frequency filtering (3–13 Hz), statistical predictive deconvolution, and automatic gain correction [*Berhorst*, 2006].

[11] Seismic phases identified in record sections of profile NIC-20 are interpreted to correspond to diving waves traveling through the sediments (P_s) and overriding (P_g) and subducting plate crust (P_{sc}), those traveling into the oceanic (P_n) and overriding-plate upper mantle (P_{mw}), and wide-angle reflections at the inter-plate boundary (P_iP), and the subducting plate (P_mP) and upper-plate crust-mantle boundaries ($P_{mw}P$). In this work, we

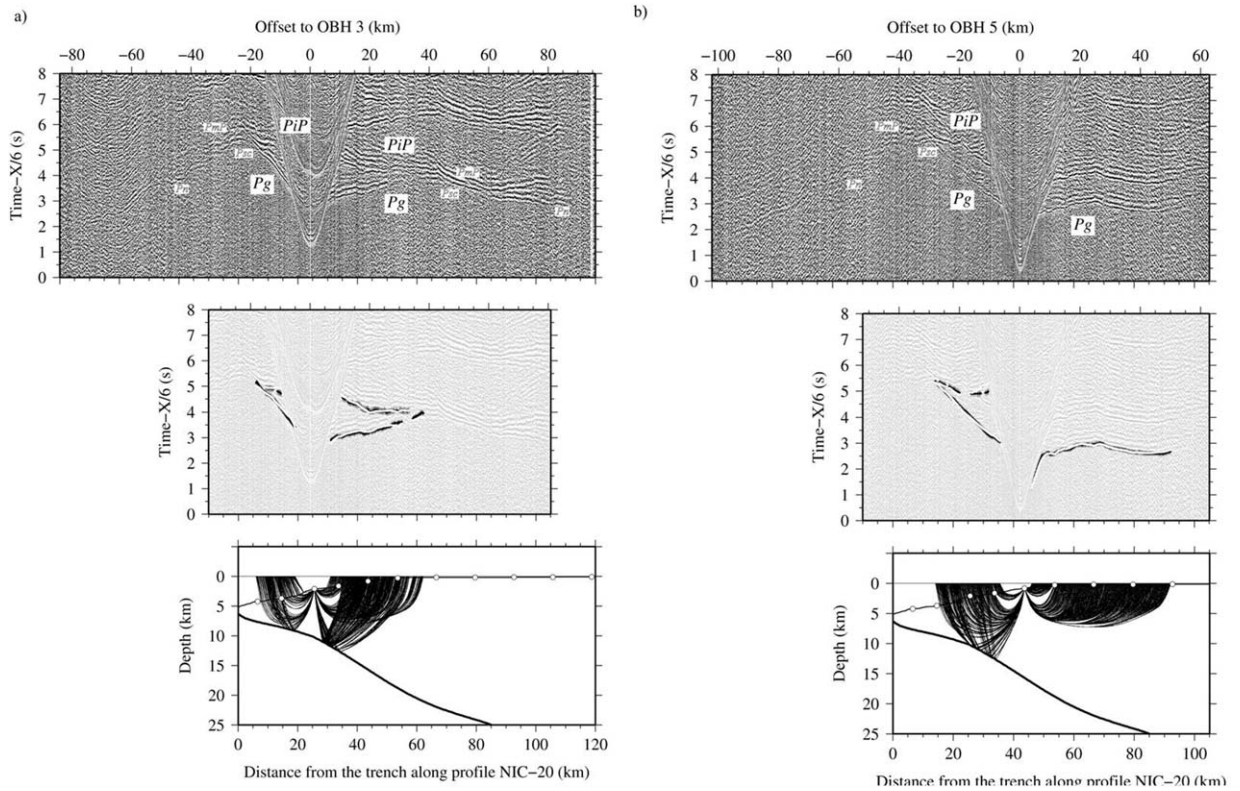

Figure 2. From top to bottom, record sections, travel time fitting, and ray paths corresponding to OBHs number (a) 3, (b) 5, (c) 7, and (d) 9, as well as landstation number (e) 2, along WAS profile NIC-20 (Figure 1). The seismic phases of interest are the refraction through the sediments and the overriding plate crust (P_g), the reflection at the inter-plate boundary (P_iP), in the case of the OBH, and the reflection at the base of the crust under the Sandino basin ($P_{mw}P$) and the refraction within the top of the upper-plate mantle wedge (P_{mw}), together with P_g, in the landstation. In addition, seismic phases refracted through the subducting crust (P_{sc}) and uppermost mantle (P_n), and reflected at the base of the subducting crust (P_mP) are also shown in the OBH record sections, though not included in the inverted data set. In the ray path plot, the thick black lines show the inverted inter-plate and upper-plate Moho reflectors, and white circles display receiver locations.

focus on the structure of the continental margin basement and the geometry of the inter-plate boundary, so that to constrain it we need only phases traveling through the overriding plate (P_s, P_sP, P_g, P_iP, $P_{mw}P$, and P_{mw}), and excluded from the inversion phases crossing the inter-plate boundary and traveling into the oceanic plate. The reason for this strategy is twofold. First, the velocity field of the subducting plate cannot be inverted within reasonable uncertainty bounds using P_{sc}, P_mP, and P_n with conventional acquisition geometries because rays traveling through the subducting crust correspond to a limited range of ray parameters (i.e., poor azimuthal coverage) so that the corresponding system of ray equations is underdetermined. Second, the high velocity uncertainty of the subducting crust can also affect the velocity field of the overriding plate. These effects have been already noted in previous works [e.g., *Sallarès and Ranero*, 2005; *Lefeldt et al.*, 2012], and confirmed by inversion tests made with and without the subducting plate phases.

[12] Figure 2 shows five record sections with the interpreted seismic phases corresponding to four OBHs and one landstation. The P_g phase is observed in all the stations to offsets varying from less than 10 km for the OBH closest to the trench axis up to a maximum of ~70 km at the OBH deployed in the upper slope (Figures 2a–2d) and at the land stations (Figure 2e). Apparent velocities for this phase range from ~2 km/s at the seafloor to ~4 km/s at the base of the overriding plate under the lower slope, and ~2 km/s at the top and ~6 km/s at the base under the upper slope. Concerning the reflected phases P_iP and P_mP it is easy to distinguish between them in the record sections of the OBH located from the mid slope to the trench (e.g., OBH 3 and OBH 5 in Figures 2a and 2b). For the rest of OBH it is more difficult to distinguish between these two seismic phases,

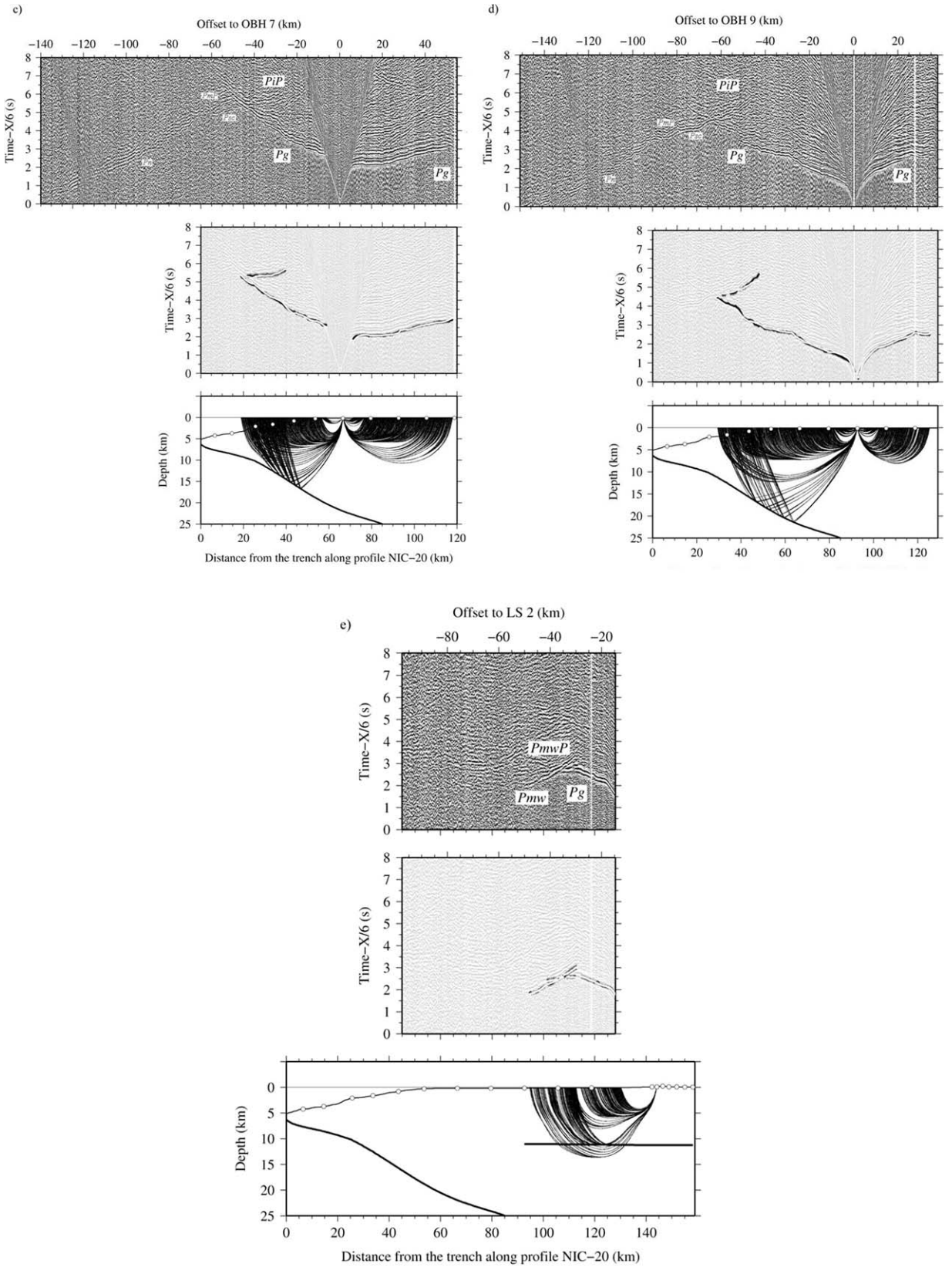

Figure 2. (Continued)

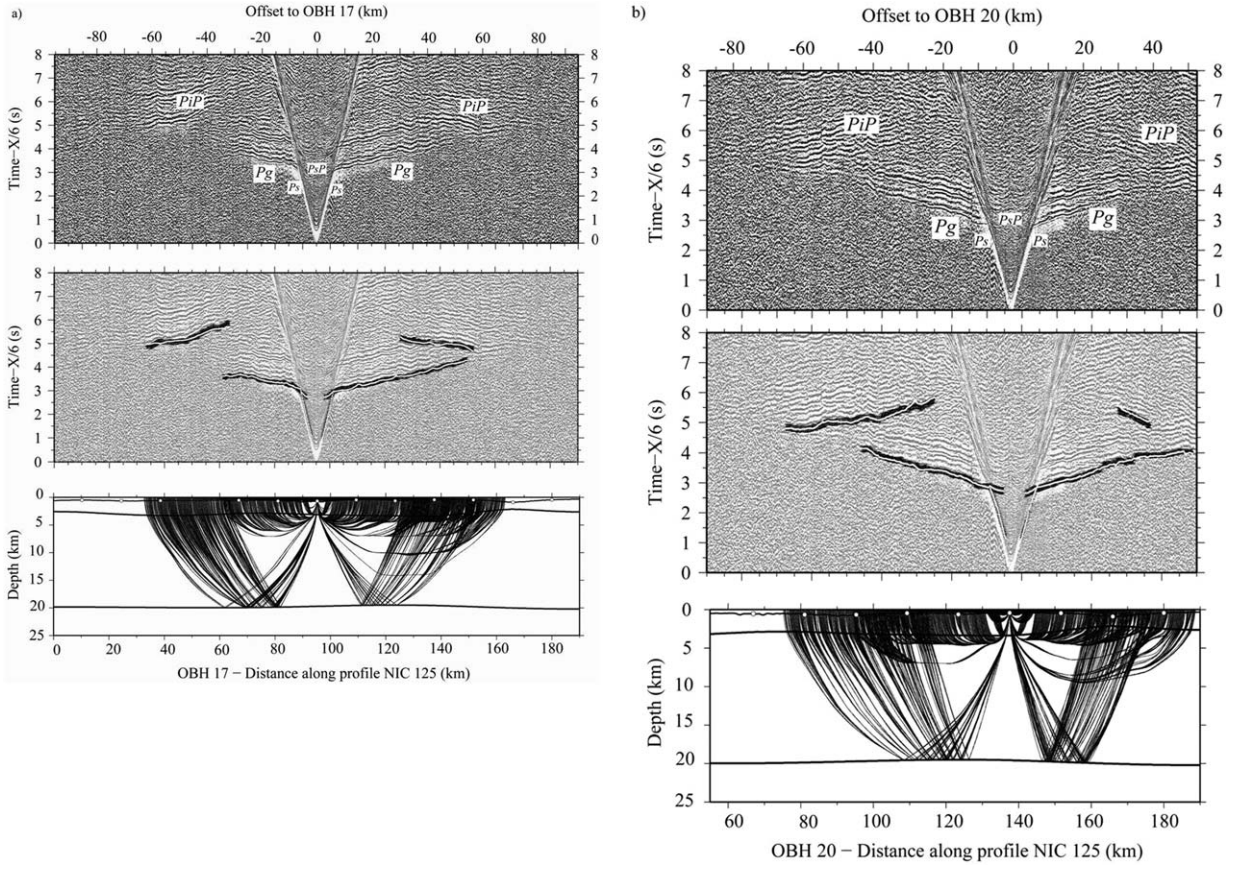

Figure 3. From top to bottom, record sections, data fitting, and ray paths corresponding to OBHs number (a) 17 and (b) 20 along WAS profile NIC-125 (Figure 1). The seismic phases of interest are the refraction through sediment (Ps) and overriding plate crust (P_g), and the reflections at the sediment-basement (PsP) and inter-plate (P_iP) boundaries. From top to bottom in the ray path plot, the thick black lines show the inverted sediment-basement and inter-plate reflectors, white circles display receiver locations.

especially in the landward part of the record sections because the slab is deeper and the apparent velocity is higher. In this case we have checked for travel time reciprocity in common shot-receiver pairs at different OBHs as a guide to identify and pick them. In contrast to NIC-20, the record sections of the trench-parallel NIC-125 profile have all very similar phases P_s, P_g, P_sP and P_iP phases, with no clear seismic phases crossing the inter-plate boundary identified. The record sections of two OBHs from NIC-125 display typical P_s and P_g phases observed in all stations to offsets of 70–80 km (Figure 3). Apparent velocities for those phases are similar in all record sections, ranging from ∼2 km/s at the seafloor to ∼6 km/s at the bottom.

[13] The P_g phase is asymptotic to a secondary arrival, which we have identified as the P_iP, that is observable in every OBH along the continental slope, with the exception of OBH 6 in NIC-20. The arrival times of P_iP increase progressively with OBH distance from the trench axis (Figures 2a and 2b), reflecting the dip of the plate interface along this trench-perpendicular profile. Contrary to NIC-20, the arrival times of P_iP do not show significant variations in the record sections of NIC-125, indicating that the depth to the inter-plate boundary does not change substantially along the trench-parallel profile (Figure 3). An interesting observation particularly clear in two record sections of NIC-125 is the presence of a shadow zone between the P_g and P_iP phases (Figure 3). Similar shadow zones have been described in other subduction zones associated to either a low-velocity zone or a zone with small vertical velocity gradient, just above the reflecting plate interface [e.g., *Sallarès and Ranero*, 2005].

[14] The P_g and P_iP phases identified in record sections along NIC-20 and NIC-125 form the data set

inverted for seismic structure and intra-plate geometry. In addition, we have included two other phases visible in record sections of the land stations along NIC-20 that arrive earlier than P_iP (Figure 2e). These phases should correspond to a reflection within the overriding plate, and to the corresponding refraction within the layer immediately below. The apparent velocity of the refracted phase exceeds 7.5 km/s, so we have tentatively interpreted it as a refraction within the upper-plate mantle wedge (P_{mw}), and the reflected phase as a reflection at the Moho above the mantle wedge ($P_{mw}P$).

[15] The arrival times of the seismic phases described above were picked manually in the record sections of the two profiles. The final data sets are composed of 7007 picks corresponding to first arrivals (P_g and P_{mw}), and 1335 corresponding to reflected phases (P_iP and $P_{mw}P$) along NIC-20, and by 6540 first arrivals (P_s and P_g), and 3748 secondary arrivals (PsP and P_iP) along NIC-125. Picking errors were assummed to be of the order of half a dominant period of the picked phase ($\sim$10 Hz) to account for a possible systematic shift in the picking. Depending on the seismic phase the assigned picking uncertainty varies between 50 ms (P_g) and 75 ms (P_iP).

[16] MCS lines coincident with the WAS ones were also acquired during EW00–05 survey, using a 6 km long streamer configured to record at 240 channels with a sampling rate of 2 ms. The seismic source was an airgun array consisting of 20 airguns adding up to a volume of 112 L and the shot spacing was 50 M. The MCS processing sequence applied includes elimination of noisy traces, spherical divergence correction and statistical predictive deconvolution, and far- and near-trace mute, stack, time and space variant band pass filter, and Forbush decrease (FD) poststack time migration [*Berhorst*, 2006; *McIntosh et al*., 2007].

3.2. Joint Refraction and Reflection Travel Time Inversion Method

[17] The 2-D models of seismic velocity distribution and reflector's geometry were obtained by joint refraction and reflection travel time inversion of the data picked along the two WAS profiles. For the inversion we used the *tomo2d* code [*Korenaga et al*., 2000]. The velocity models consist of a sheared mesh of velocity nodes, with variable spacing both vertically and horizontally, which hangs from the seafloor. The code also allows inverting for the position of a floating reflector, which is parameterized by an independent array of nodes each having the vertical degree of freedom. The forward problem is solved by calculating the ray paths using a hybrid method combining the graph method [e.g., *Toomey et al*., 1994] and the ray-bending method for refinement [*Papazachos and Nolet*, 1997; *van Avendonk et al*., 1998]. The travel times are subsequently obtained by integrating the slowness along the ray path. The inverse problem is solved by inverting the linearized forward problem using the least square residuals (LSQR) sparse matrix solver algorithm [*Paige and Saunders*, 1982]. In order to avoid inversion instabilities the Fréchet matrix is modified to incorporate some regularization constraints. This regularization constraints include smoothing matrices represented by correlation lengths applied to both velocity and depth perturbations, and damping matrices to limit the average perturbation in both velocity and depth parameters at each iteration. The ray coverage is indicated by the derivative weight sum (DWS) which is the column-sum vector of the Fréchet velocity kernel, and a quantitative measure of the density of seismic rays traveling near a certain node [*Toomey and Foulger*, 1989]. Thus the DWS can be used to mask the final model as it estimates the ray coverage that is related to the linear sensitivity of the inversion.

[18] To obtain the velocity models shown in Figure 4, we followed a top-to-bottom layer-stripping strategy, which consists on inverting one layer at a time and is analogous to that described in *Sallarès et al*. [2011, 2013]. "A layer" is here defined as the section of the model comprised between two consecutive reflectors. The seismic phases used in the inversion are the reflection from the base of the layer and the phases refracted in the layer. These two phases together give information on the velocity distribution within the layer and the geometry of its base.

[19] Along profile NIC-20 the first inverted layer includes the overriding plate and sediments, from the seafloor to the inter-plate boundary under the lower and middle slope, and from the seafloor to the overriding-plate Moho under the upper slope and shelf. Therefore the phases used in the overriding-plate inversion are P_s, P_g, and P_iP/$P_{mw}P$. The inverted model is then inserted into an extended one that includes the upper-plate mantle wedge (P_{mw} phase). We did not identify any basal reflector beneath the mantle wedge. Sedimentary reflections are clearer in NIC-125 than in NIC-20, so we performed a first inversion of the sedimentary layer (P_s and P_sP phases), and a second one

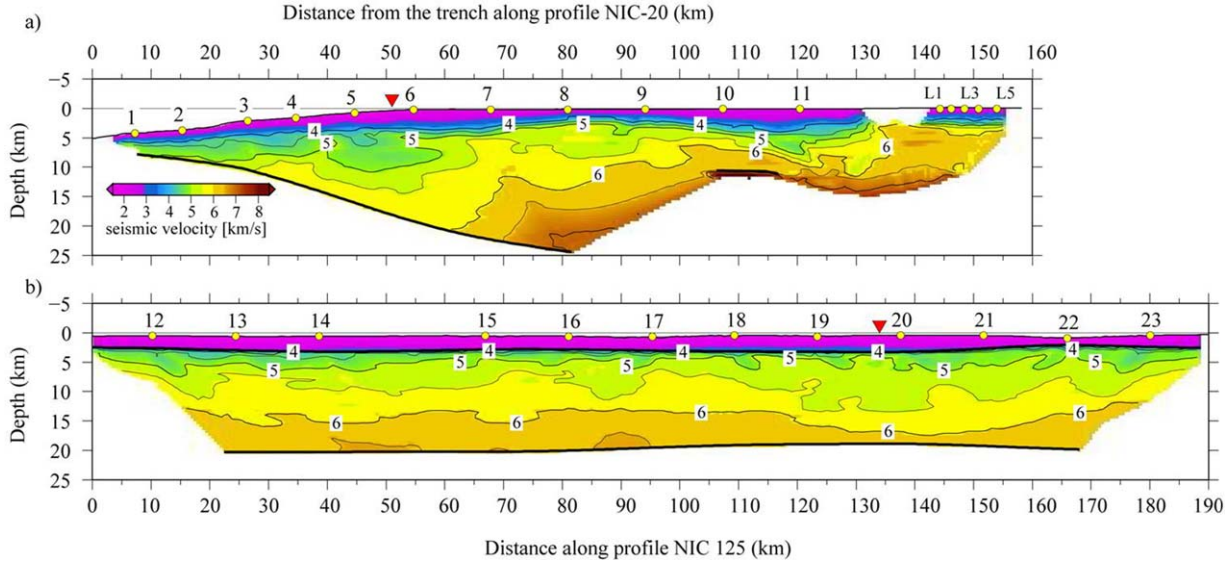

Figure 4. (a) *P* wave velocity model of the overriding plate and geometry of the inter-plate boundary reflector along WAS profile NIC-20 (see Figure 1 for location). The model has been obtained by joint reflection and refraction travel time inversion using the *tomo2d* code [*Korenaga et al*., 2000]. Inter-plate and upper-plate Moho reflectors are represented by thick black lines. Yellow circles on the seafloor mark the positions of the OBH and land stations and the red triangle indicates the intersection with profile NIC-125. Isovelocity contours in the sediments are not shown for clarity.(b) Same as Figure 4a but for the WAS profile NIC-125 (Figure 1). Inter-plate and sediment-basement reflectors are represented by thick black lines.

for sediments and basement (P_s, P_g, and P_iP phases). The main advantage of this procedure is that it allows to define the velocity and depth parameters with the minimum trade-off possible to keep abrupt velocity contrasts between layers in successive iterations, and thus obtain velocity models more appropriate for geological interpretation. The model parameters of the layers inverted in previous steps are overweighed in the new inversion, therefore promoting changes in the bottom layer. Reference models for the geometry of the inter-plate boundary and the velocity distribution for the sediments and the basement of the overriding plate were built for the two profiles by forward modeling of the picked travel times using the *Rayinvr* code [*Zelt and Smith*, 1992]. Horizontal grid spacing for the velocity model is 0.5 km whilst the vertical one increases with depth from 0.05 to 0.5 km. Reflector depth nodes are 0.5 km spaced. The correlation lengths increase linearly from 2 km at the top to 7 km at the bottom in the horizontal direction, and from 0.5 km at the top to 1.5 km at the bottom in the vertical direction. Different damping values were tested finally choosing 10% for both velocity and depth perturbations.

[20] As a second step for the inversion of profile NIC-20, the overriding crust model was inserted into an extended model including the overriding-plate upper mantle below the upper slope, so we added the P_{mw} phases to the data set. The inversion parameters and velocity grid spacing were the same as in the previous step. The inter-plate reflector inverted in the first step was used as starting reflector in this step. The final RMS travel time residual is 43 ms for the first arrivals (P_s, P_g, and P_{mw}) and 63 ms for the reflections phases (P_iP and $P_{mw}P$) in profile NIC-20, and 48 ms for first arrivals (P_s and P_g) and 66 ms for the P_iP reflection in profile NIC-125.

3.3. Uncertainty of the Model Parameters

[21] A statistical analysis was performed to estimate the uncertainty of the velocity and reflector depth parameters along the two profiles. The method is analogous to that implemented by *Korenaga et al*. [2000], which is based, in turn, on that originally proposed by *Tarantola* [1987]. The procedure starts by randomly perturbing the two travel time data sets within a range of 70 ms corresponding to the addition of common phase error (30 ms), common receiver error (20 ms) and individual picking errors (20 ms) to create 500 perturbed, noisy data sets that take into account the different errors that may add up during phase picking. In addition, the seismic velocity distribution and the geometry of the reflector of both final models were randomly

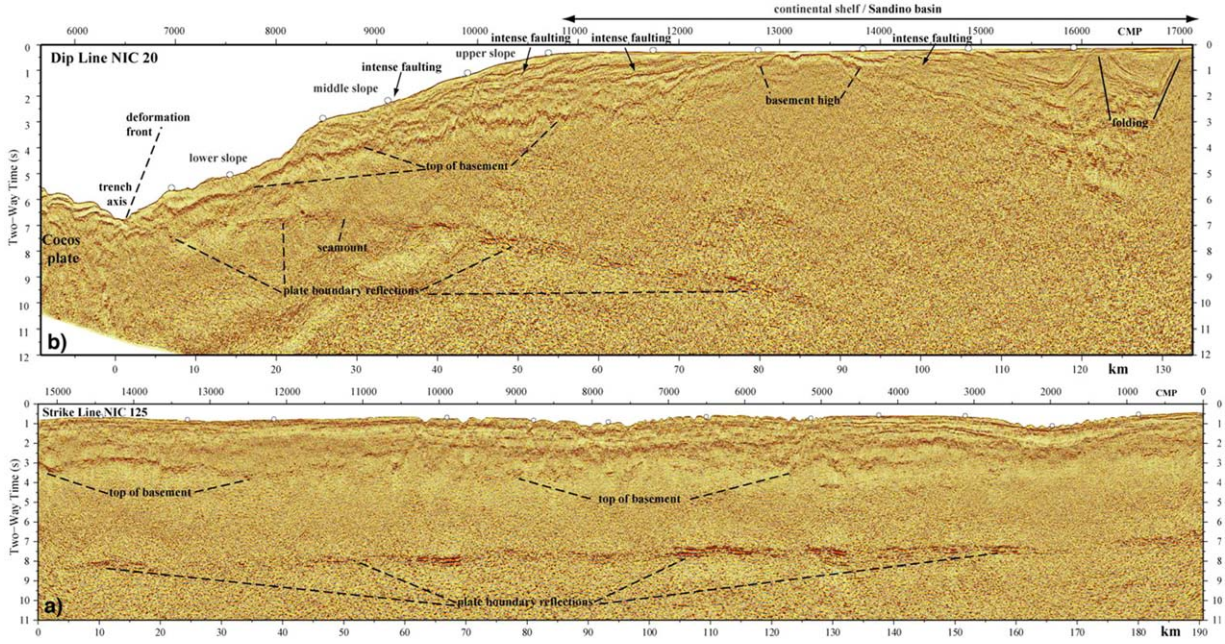

Figure 5. (a) Poststack time-migrated MCS reflection strikeline NIC 125 shot along the slope offshore Nicaragua. The image shows the good continuity of plate boundary zone reflection that change abruptly of amplitude along the margin. The slope sediment overlies a basement that is fairly featureless. The image shows that the regional structure is fairly two-dimensional. (b) Poststack time-migrated MCS reflection dip line NIC 20, collected perpendicular to the continental margin. The image shows the continuity of the plate boundary reflective zone. The top of basement is marked by a clear reflection under the slope, showing a pronounced thinning toward the trench axis. The Sandino basin is compartmentalized in two sub-basins by an uplifted basement high. The region is cut by abundant normal faults.

perturbed as well to generate 500 different initial models. The perturbation range for the velocity was ± 0.5 km/s. The inter-plate boundary of profile NIC-20 was perturbed by randomly varying its dip angle within a range of 8° (14° $\pm$ 4°), while that of profile NIC-125 was perturbed within a ± 2 km depth range. The next step was to conduct an inversion for each model—data set pair, using the inversion parameters mentioned in the previous subsection. According to *Tarantola* [1987], when the initial models cover all the region of non-null probability within the space of parameters, the average resulting model is the most probable solution and the final standard deviation is a statistical measure of the model parameters uncertainty.

4. Results

4.1. Multichannel Seismic Images of the Convergent Margin and Plate Boundary

[22] The two MCS profiles coincident with the two WAS lines provide detailed images of the structure of the continental margin and plate boundary zone that complement the information in the velocity models. The images display the tectonic structure and stratigraphy of the slope sediment, the tectonic structure of the basement of the margin, the dimensions of a frontal sediment prism, and display the reflective character of the plate boundary (Figures 5 and 6).

[23] The trench-perpendicular line NIC-20 shows the structure under the continental shelf and slope. The bulk of the overriding plate is formed by a rock body that displays little internal reflectivity and is bounded at top and bottom by comparatively clear high-amplitude reflections (Figure 5b). This rock body corresponds to a high velocity body in the wide-angle velocity models and is similar in character to the so-called margin wedge, described across Costa Rica [e.g., *Ranero and von Huene*, 2000; *von Huene et al*., 2000] and further NW in Nicaragua [*Ranero et al*., 2000, *Walther et al*., 2000]. The high velocities, and drilling and dredging samples have led to the interpretation that the margin wedge is formed by igneous rock probably forming part of the Caribbean flood basalt province [*Ranero et al*., 2007]. The strike line

NIC-125 displays well the lateral continuity of the margin wedge that shows little variability in character and a fairly featureless internal reflectivity (Figure 5a).

[24] Overlying the margin wedge under the shelf region are sediments of the Sandino Basin, although the inner shelf and outer shelf are separated by an intervening basement high (Figure 5b). The sediment of the Sandino basin extends under the continental slope and progressively thins downslope from ~2 s two-way time (TWT, roughly 1.8–2.2 km thickness) under the shelf edge, to a few hundreds of meter under the slope toe. Line NIC-125 shows the lateral continuity of the mid slope stratigraphy (Figure 5a).

[25] The top of the margin wedge reflection can be traced from under the shelf to under the lowermost continental slope, where it extends under the slope toe to about 1–2 km of the deformation front located at edge of the overriding plate (common midpoint, CMP ~6500 in Figure 5a). The 1–2 frontal km of the upper plate are formed by a sediment prism that resembles the frontal prism drilled offshore Nicoya Peninsula. There, the prism is 5–10 km wide and is made of reworked upper-plate sediment because all incoming sediment in under thrust [*Kimura et al.*, 1997].

[26] The plate boundary is marked by a series of reflections of variable amplitude that change in character from under the slope to under the shelf region, where they become undifferentiated at CMP 13,500–14,000 at about 11 s TWT (Figure 5b). Under the frontal ~5 km of the lower slope, the image displays well the under-thrust sediment package (CMP ~6500–6900 in Figure 5b). Further landward, lower-frequency reflections exhibiting abrupt lateral changes in amplitude characterize the plate boundary reflectivity, but there are no different reflectors at the top and bottom of the underthrust sedimentary section. A gentle shoaling and thickening of the plate boundary reflections at CMPs 8300–9000 has been interpreted as a subducted seamount [*McIntosh et al.*, 2007] that is located just landward of a prominent landslide of slope sediment causing an abrupt change in seafloor dip (CMP 8000–8400 in Figure 5b).

[27] Line NIC-125 displays the lateral character of the plate boundary reflectivity under the middle slope. Similarly to the image of the plate boundary on the dip line NIC-20, the along strike images of the plate boundary display a fairly continuous reflectivity with abrupt changes in amplitude (Figure 5a). The image on strike line NIC-125 indicates that the large-scale structure of the region is fairly 2-D.

4.2. Wide-Angle Seismic Structure Along the Trench-Perpendicular Profile (NIC-20)

[28] The WAS model along profile NIC-20 includes the overriding plate sediments and crust and the uppermost section of the upper-plate mantle wedge, together with the inter-plate and upper-plate Moho reflectors (Figure 4a). The corresponding and DWS are shown in Figure 7a and 7b. The resulting velocity distribution for the continental margin shows an average vertical velocity gradient of 0.23 s^{-1} (Figure 8) and a horizontal gradient of 0.03 s^{-1} from trench to coast along the inter-plate boundary. The velocity at the toe of the margin wedge varies from ~1.8 km/s at the top to ~4.7 km/s at the bottom, while velocity beneath the upper slope, at km 75–80 along profile, ranges from ~1.8 km/s at the top to ~7.1 km/s just above the inter-plate boundary. The uppermost part of the model represents the sedimentary blanket, which overlays the igneous basement, with the top of the basement being approximately defined by the 3.8 km/s isovelocity line. The sedimentary blanket shows two main basins: one extending from lower to middle slope, which is 3–4 km thick, and the ~5 km thick Sandino basin in the continental shelf. The two basins are separated by a basement high at ~80 km along the profile, where the overriding plate is thickest (~20 km). If we accept that the $P_{mw}P$ phase actually corresponds to Moho reflections, then the basement thins abruptly landward, reaching to 5–6 km thick beneath Sandino basin (see section 5.2). At this place, velocity values of ~7.5 km/s, characteristic of altered upper mantle, are found just below the interpreted Moho reflector, which is ~10 km deep. A striking feature trenchward from the basement high, is the reduced velocity zone located between km 35–55, where velocity is 5–10% lower than in surrounding areas. The geometry of the inter-plate boundary is well constrained by the P_iP phases giving a dip angle of ~8° beneath the lower slope, increasing to 15° beneath the upper slope.

[29] The plate boundary determined from the inversion of WAS data converted to TWT shows a systematic mismatch with the reflector imaged in the coincident MCS data (Figure 6a). The largest misfit occurs in the segment located under the reduced velocity zone under the slope, where the inverted inter-plate reflector is ~1 s TWT deeper

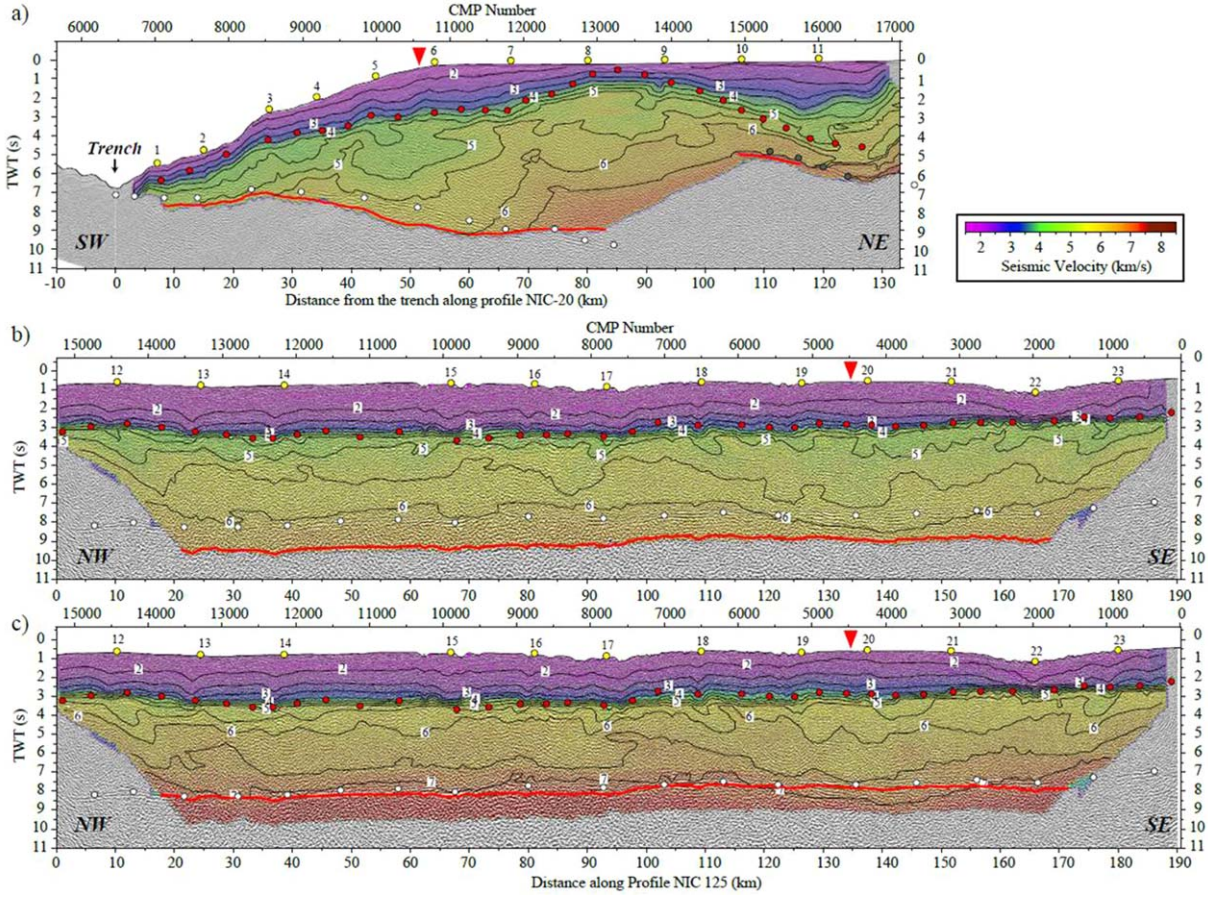

Figure 6. (a) MCS line coincident with the NIC-20 profile (Figure 4a), superimposed onto the TWT-converted *P* wave velocity model. The circles inside the model delineate the geometry of inter-plate (white) and upper-plate Moho (gray) reflections imaged on MCS records. The thick red line corresponds to the TWT-converted inter-plate boundary of the WAS model. OBHs and land stations are shown as yellow circles on the seafloor and the red triangle represents the intersection point between profiles NIC-20 and NIC-125. Note the mismatch of the inter-plate boundary from MCS images and from WAS modeling, possibly implying seismic anisotropy. (b) Same as Figure 5a but for the NIC-125 WAS and MCS profiles (Figures 4b and 5b). (c) Same as Figure 5b but having increased the velocity values of the NIC-125 model (Figure 5b) by 15% to account for seismic anisotropy and match the MCS image of the inter-plate boundary.

than the reflection in the MCS image. The MCS data images a reflector at CMP ~16,000 at 5–6 s that matches an abrupt increase in velocity gradient (~6.5 to ~7.5 km/s in ~1 km at this point) that corresponds well with the location of the modeled upper-plate Moho beneath Sandino basin (Figure 6a).

[30] The velocity uncertainty throughout the western sector of the profile is smaller than 0.1 km/s in the first ~3 km beneath seafloor (Figure 7a), except below the lower slope where low uncertainty reaches ~10 km under the seafloor, near the inter-plate boundary. Away from this region, velocity uncertainty gradually increases to ~0.2 km/s just above the inter-plate boundary from close to the trench to about 50 km away, where the inter-plate reflector is more than 15 km deep. For the rest of the western sector the uncertainty is lower than 0.3 km/s. The eastern sector, especially from km ~130 to the end of the profile, is less constrained, due to the limited azimuthal coverage (Figure 7b). Here uncertainty values are ~0.2–0.3 km/s, with local values near 0.35 km/s. However, the steep gradient, the upper mantle velocities, and geometry of the inter-plate reflector in this sector of the model are reasonably well constrained for their interpretation. A particularly well-resolved structure is the segment below the low-velocity zone, where a there is a shoaling of the inter-plate boundary. Thus, the results indicate that the overall velocity distribution is well constrained throughout the trench-perpendicular profile, with

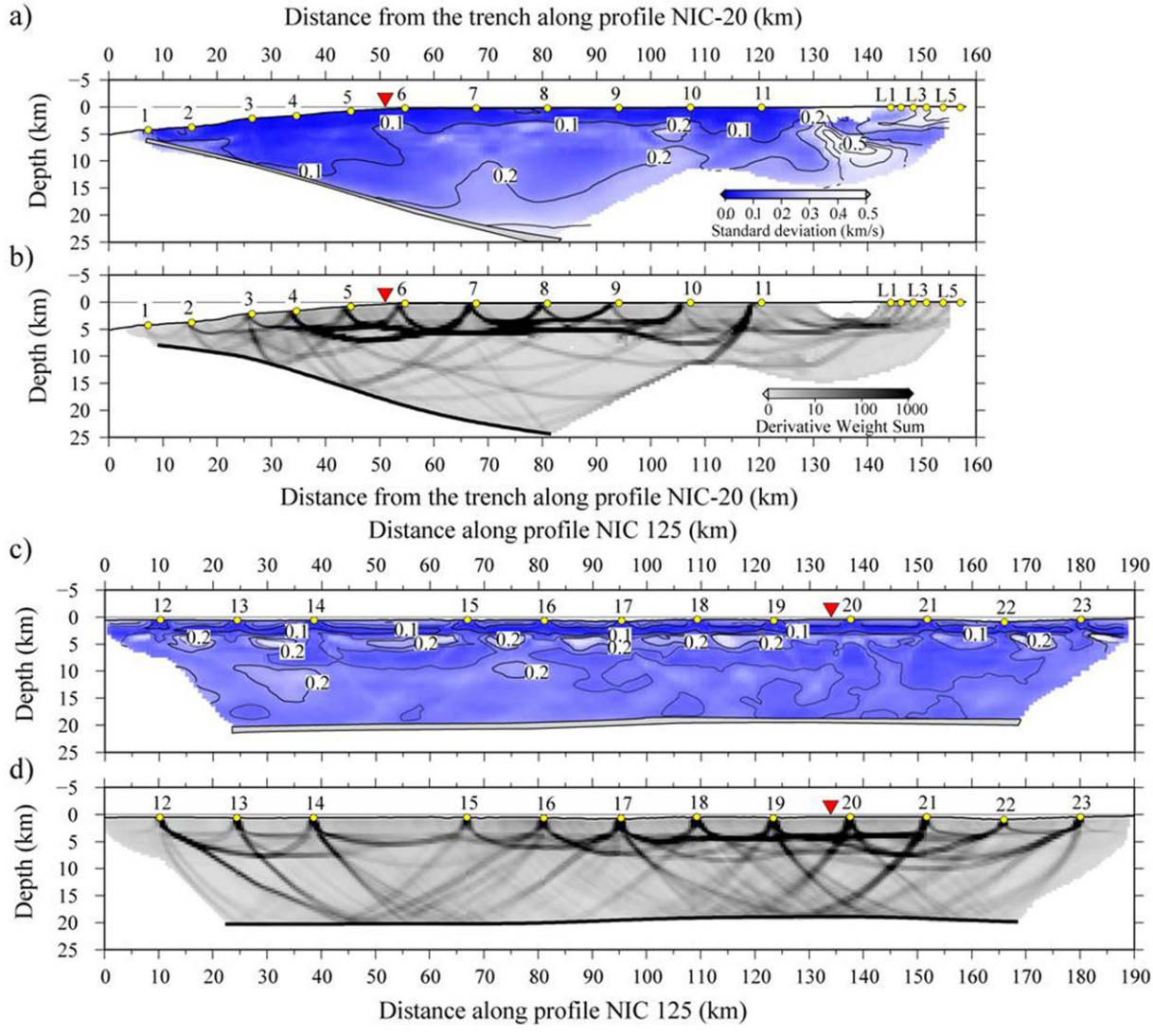

Figure 7. (a) Statistical uncertainty model of the *P* wave velocity values and the geometry of the inter-plate boundary for the NIC-20 model displayed in Figure 4a. Details on the calculation are given in the text. (b) Derivative weight sum (DWS) values obtained along the NIC-20 model. (c) Same as Figure 7a but for the NIC-125 model displayed in Figure 4b. (d) Same as Figure 7b but for the NIC-125 model.

unconstrained regions are restricted to localized areas, particularly in the easternmost sector of the model in the offshore-onshore transition.

4.3. Wide-Angle Seismic Structure Along the Trench-Parallel Profile (NIC-125)

[31] The WAS model along the strike profile NIC-125 includes the sediments and the basement that display a laterally more uniform velocity structure and depth to the inter-plate boundary than NIC-20 (Figure 4b). The sedimentary layer is 3–4 km thick and shows velocity varying from ~1.8 km/s at the top to ~3.8 km/s at the base. The top of the basement is characterized by a strong velocity gradient that give way to a vertical velocity gradient of 0.2 s^{-1} with an average velocity of 4.0–4.2 km/s at the top and 6.2–6.4 km/s at the bottom (Figure 8). The gentlest gradient is at the base of the upper plate, where it may cause the shadow zone between the P_g and P_iP phases (Figure 3). The lowest basement depth-velocity relationship is at km ~135 along profile around the crossing with dip line NIC-20. The inter-plate boundary is subhorizontal, so that the entire overriding plate has a constant along-strike thickness of 17–18 km. The comparison between the WAS model converted to TWT and the MCS image shows a systematic ~1 s TWT mismatch at the inter-plate boundary interface (Figure 6b), as

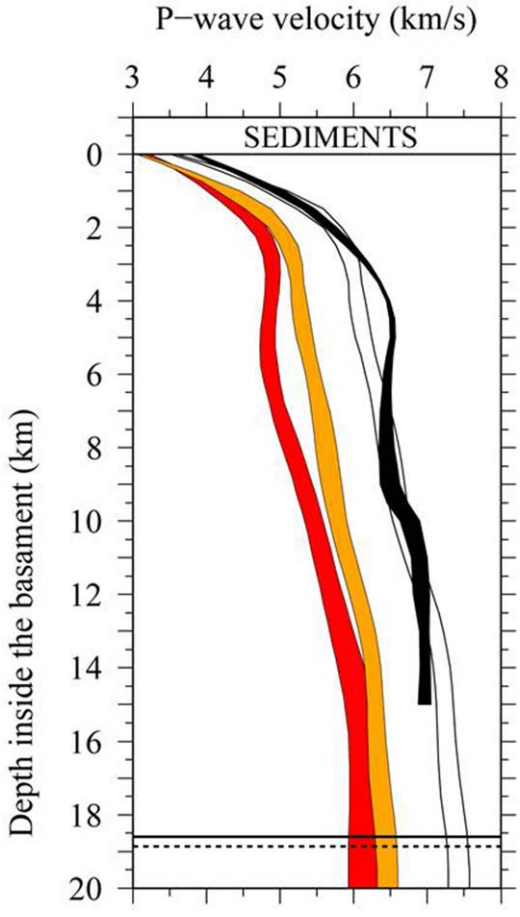

Figure 8. 1-D velocity profiles extracted from both velocity models (Figure 4). Red and orange bands correspond to NIC-20 and NIC-125 profiles, respectively, at their intersection. The velocity profile represented as a white band was obtained increasing the velocities of the orange band by 15%. The black band is a reference corresponding to a 1-D velocity profile extracted from a WAS model of the thick crust of the aseismic Carnegie Ridge formed at the Galapagos Hotspot [*Sallarès et al*., 2005]. The horizontal lines mark the depth of the inter-plate reflectors for NIC-20 (solid line) and NIC-125 (dashed line) at the intersection point.

observed on dip line NIC-20 (Figure 6a). We discuss three possible explanations for this difference in travel times between the WAS and MCS reflections. A first possibility is that they represent different boundaries like inter-plate boundary in MCS data and oceanic Moho in WAS data. Assuming an average velocity of 6–7 km/s, the 1 s TWT misfit implies a 3.0–3.5 km thick subducting crust, which is much thinner than the ∼5.5 km thick incoming-plate crust [*Ivandic et al*., 2008] measured on the prolongation of NIC-20 (labeled p50 in Figure 1a). Alternatively, WAS data could be mapping an intraoceanic-crust reflector, but OBH records of the incoming plate do not show intracrustal reflections comparable to the conspicuous PiP phase [*Ivandic et al*., 2008]. Additionally, it seems unlikely that the two methods image two different, comparatively high acoustic impedance reflectors at the same spatial location. Our preferred interpretation is that the velocity measured with the two methods differ due to seismic anisotropy, and that subhorizontal propagation of WAS long-offset phases occurs at lower velocities than near-vertical propagation in smaller-offset MCS records. A 15% seismic anisotropy provides the best match between MCS and WAS reflections with a root-mean-square (RMS) overall difference between locations of the inter-plate reflections of 0.25 s TWT for NIC-20 (Figure 6c).

[32] Velocity uncertainty along NIC-125 is similar to NIC-20 (Figure 7c). It is smaller than ∼0.1 km/s in the sedimentary layer (upper 3–4 km) and then it increases to 0.2–0.3 km/s at the sediment-basement boundary reflecting the characteristic steep gradient of this interface. The velocity in upper third of the basement is essentially controlled by intracrustal refractions (Figure 7d), with uncertainty <0.2 km/s, increasing to 0.2–0.3 km/s toward the lower half of the basement, where both velocity and inter-plate geometry are resolved solely by P_iP phases (Figure 7d). This means that there is a trade-off between location of the reflecting interface and velocity above, increasing uncertainty in both parameters. Nonetheless, uncertainty of inter-plate boundary location is <0.5 km, well below the standard deviation of the initial models considered, and together with a similar uncertainty for the velocity implies that both parameters are well resolved.

5. Discussion

[33] In this section, we interpret the seismic structure and physical properties of the overriding plate based on the models shown in Figures 4–6, starting with the overriding-plate basement under the lower and mid slopes, and continuing with the basement under the upper slope and continental shelf. We use gravity modeling of velocity-derived density structure to further constrain the nature of the upper-plate rocks. We then integrate the MCS images to interpret the tectonic structure and hydrogeological system of the upper plate. Subsequently, we relate the structure and physical properties of the overriding plate, and location of the mantle wedge with the interpreted location of

the downdip limit of the seismogenic zone. Finally, we discuss the potential relationship between the structure of the upper plate and relief of the inter-plate boundary to the anomalous tsunamigenic character of the 1992 tsunami earthquake.

5.1. The Nature of the Overriding Plate Basement

[34] The velocity model of NIC-20 described in section 4.1 shows a steep velocity gradient from top to bottom and from the trench axis toward the coast (Figure 4). The strong lateral and vertical gradient has been observed previously described in different convergent margin, and concretely in other sectors of the MAT including Costa Rica [*Ye et al*., 1996; *Stavenhagen et al*., 1998; *Christeson et al*., 1999; *Sallarès et al*., 1999, 2000] and northern Nicaragua [*Walther et al*., 2000]. To interpret the meaning of these gradients it is important to know the nature of the overriding plate basement. The current interpretation of the Central America margin along the MAT in that along Costa Rica, Nicaragua and Guatemala, subduction is dominated by tectonic erosion, and the basement is made of igneous rocks [e.g., *Ranero and von Huene*, 2000]. Dredging of the igneous basement rock and sediment offshore Nicaragua outcropping at the middle slope [*Silver et al*., 2000] provide constraints on the basaltic nature of the margin wedge and the timing of first deposit of fore-arc sediment, during Late Cretaceous time, similar to Nicoya Complex in Costa Rica [*McIntosh et al*., 2007]. MCS profiles of EW00–05 survey (Figure 1), indicate that the Nicaraguan margin is similar to Costa Rica [*McIntosh et al*., 2007], with a high-velocity margin wedge beneath the trenchward-thinning sedimentary cover. None of the MCS profiles show evidence of an accretionary wedge fronting the margin. The rough surface that characterizes the top of the igneous basement typically extends to <1 km from the trench [*McIntosh et al*., 2007], as observed in MCS profile NIC-20 (Figure 6a). A WAS profile collocated with p80 profile (Figure 1a) shows a velocity structure similar to the NIC-20 model, with velocity of $\sim$4 km/s at the top of basement, increasing with depth and distance from the trench to values of $\sim$6.5 km/s at the base of the overriding plate under the upper slope [*Walther et al*., 2000]. These authors interpreted the velocity reduction toward the trench as an effect of trenchward-increasing fracturing and fluid alteration of the igneous basement.

[35] Assuming that the basement is of igneous nature and of similar rock composition, the strong velocity gradient in NIC-20 (Figure 4a) should reflect changes in the degree of rock fracturing and alteration. One can estimate the degree of rock fracturing/porosity (Φ) from *P* wave velocity (α) using existing effective medium theory relationships [e.g., *Mukerji et al*., 1995], following the approach applied to estimate the level of structural integrity of the erosional margin offshore Antofagasta, North Chile [*Sallarès and Ranero*, 2005]. The parameters needed to estimate Φ as a function of α are the critical porosity (Φ_c), which represents a porosity threshold value above which the rock is fluid supported, so it is not able to transmit loads or stresses, the velocity of the unaltered rock, α_R, and the rock velocity at Φ_c, α_c. According to experimental results, and taking the values in our model, $\alpha_R \approx 6.5$ km/s, $\alpha_c \approx 4.3$ km/s, and $\text{ø}_c \approx 0.15$ [*Nur et al*., 1998; *Sallarès and Ranero*, 2005]. Thus, assuming that the overriding plate basement is made of igneous rocks similar to oceanic basalt, the parts of the margin with velocities lower than $\sim$4.3 km/s ($\text{ø} > 0.15$) have to be mostly disaggregated and fluid supported. In contrast, for velocity higher than $\sim$4.3 km/s ($\text{ø} < 0.15$), rock porosity can be estimated using the values of α_R, α_c, and ø_c as referred above, so that $\Phi = 0.46 - 0.07\alpha$ Additional details on the calculations can be found in *Sallarès and Ranero* [2005].

[36] Figure 9 shows estimated upper-plate porosity/fracturing along NIC-20 using the velocity model of Figure 4a. Porosity uncertainty values propagated from the statistically derived velocity uncertainty (Figure 7a) are smaller than 1% within most of the upper plate, and $1-2$% near the inter-plate boundary, being negligible for inferences of material physical properties and related tectonic processes. Porosity estimations indicate that the $\sim$5 frontal km excluding the first $\sim$1 km of accretionary prism of the margin correspond to highly fractured, likely partially disaggregated basement. The rest of the margin wedge is constituted by rocks where the degree of fracturing decreases progressively from $\sim$15% to almost 0% at $\sim$70 km from the trench axis (Figure 9). Similar structure and rock properties have been observed in other erosional convergent margins such as North Chile [*Sallarès and Ranero*, 2005].

[37] The low-velocity zone between 35 and 65 km along the profile (Figure 4a), is associated to a porosity increase of 2–3% compared to neighboring areas (Figure 9) and is located where the WAS

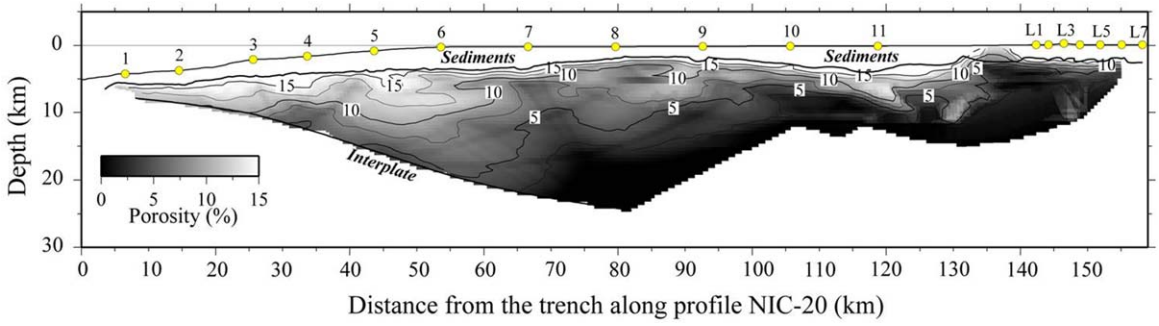

Figure 9. Porosity model calculated using the *P* wave velocity model along the NIC-20 profile (Figure 4a). To convert velocity into porosity we have assumed that the basement of the overriding plate is made of igneous rocks (basalts) and have applied an empirical relationship based on data compilation for this rock type [*Nur et al*., 1998]. Sediments are excluded from the calculation.

and MCS inter-plate reflections display the largest mismatch in TWT. This mismatch can be explained by an anisotropy of ∼15% between subvertical and subhorizontal propagation velocity (Figure 6c). Experimental evidence and numerical models indicate that *P* wave velocity is more strongly decreased when elongated fractures have their long axis perpendicular to the propagation direction. Numerical tests show that, depending on the *P* wave frequency, the anisotropy between perpendicular and parallel incidence may vary by as much as 30% [*Carcione et al*., 2012]. The slower wide-angle propagation velocity compared to near-vertical propagation (Figure 6) indicates that fractures under the slope should be elongated in a subvertical direction. These fractures may represent paths for fluids to migrate from the subducted slab toward the seafloor. Similar upper-plate low-velocity anomalies have been observed in North Chile [*Sallarès and Ranero*, 2005] and Ecuador [*Gailler et al*., 2007] using WAS data. It is noteworthy that, once corrected for velocity anisotropy, the 1-D velocity profile at the lines intersection (Figure 8) closely resembles that of aseismic volcanic ridges described in different parts of the Galápagos Volcanic Province [*Sallarès et al*., 2003, 2005], which can be considered the reference velocity model for nonfractured upper-plate basaltic basement.

5.2. The Sandino Fore-Arc Basin and the Upper-Plate Mantle Wedge

[38] The basement is covered by a 1–5 kmthick sedimentary layer that extends along the margin from the lower slope to onshore. This sediment cover is separated in two main basins. The outer basin is up to 3–4 km thick and extends across the upper slope and outer shelf to the basement high located at ∼80 km from the trench, which separates the two basins. The seismic data show (Figure 6a), that sediment thins rapidly from under the upper slope to the middle slope and further into the lower slope. Landward from the basement high, an inner sedimentary basin reaches 7–8 km thickness at km ∼115 km from the trench. The sub-basin, are part of the fore-arc Sandino basin, that extends under the shelf from Nicaragua to Mexico. There is a good correspondence between a reflector under the basin imaged in the MCS profile and a steep velocity gradient from ∼6.5 to ∼7.5 km/s in less than 1 km interpreted to mark the base of the crust under Sandino basin in our model (Figure 6a). Clear reflected phases are observed in the land station recordings (Figure 2e). These $P_{mw}P$ phases define a reflector that separates crustal-like velocities of ∼6.5 km/s above from upper mantle-like velocities of ∼7.5 km/s below, suggesting the presence of thin crust (5–6 km) beneath the Sandino basin.

[39] The low velocity of the mantle wedge has been attributed to serpentinization of peridotites by fluids released from the incoming plate [e.g., *DeShon et al*., 2006]. A similar mantle velocity body beneath Sandino basin has been modeled by *Walther et al*. [2000] along the p80 WAS profile offshore central Nicaragua, some 120 km NW from NIC-20 (Figure 1). Two hypotheses have been suggested for the origin and evolution of the Sandino basin. One suggests that the Nicaragua margin represents the westernmost edge of the Caribbean plate, and that the basin originated by flexure of the upper plate as a response to the initiation of subduction in the Late Cretaceous [*Ranero et al*., 2000]. The other hypothesis argues that the basin developed in the frontal part of a

thick oceanic plateau that collided with a terrain the Nicaragua margin in the Late Cretaceous. The basin would then represent the subduction trench previous to the collision and westward jump of the subduction zone [*Walther et al*., 2000], and the high velocity body would be a remaining mantle sliver of the Cretaceous subducting slab. The WAS data indicate that a similarly thin crust and shallow mantle wedge extends along Nicaragua beneath the Sandino basin.

[40] The WAS data do not allow to map the deep structure of the mantle wedge under much of the continental shelf, because P_g and P_iP phases do not cover the deep region of the overriding plate (Figure 7b). At km ~75 the overriding plate is ~20 km thick, and both the seismic velocity and velocity gradient are comparable to those of Galápagos aseismic ridges (Figure 8). Here the velocity just above the inter-plate boundary is ~7.2 km/s, characteristic of the lowermost Layer 3 rocks [*White et al*., 1992]. Therefore, assuming that the $P_{mw}P$ phase is a Moho reflection from under the Sandino basin, then the updip limit of the mantle wedge must be located trenchward from this point (km ~100 along profile).

5.3. Gravity Constraints on Fracturing-Related Seismic Anisotropy and Nature of the Mantle Wedge

[41] As previously discussed, two key results concerning the upper plate structure are (1) the mismatch between the MCS and WAS inter-plate reflections possibly due to fracture-related seismic anisotropy, and (2) A shallow ~10 km depth reflector separating crustal-like from mantle-like velocities beneath Sandino basin that may indicate a shallow mantle wedge. To test the interpretation of the velocity model, we performed gravity modeling of velocity-derived density models using satellite-based free-air gravity anomaly data [*Sandwell and Smith*, 2009] along profile NIC-20 (Figure 10).

[42] We employed a code based on *Parker*'s [1974] spectral method as modified by *Korenaga et al*. [2001] to calculate the gravity anomaly produced by a laterally and vertically variable 2-D density model. The density model was constructed converting seismic velocity (Figure 4a) to density using different empirical velocity-density relationships for sediments, basement and upper mantle. To build a density model of the subducting plate beneath the margin, we hung from the inter-plate boundary a laterally extended averaged version of the crustal thickness and velocity model obtained along the seaward continuation of NIC-20 by *Ivandic et al*. [2008]. To calculate the density, we used *Hamilton*'s [1978] law for shale for the sediment, *Carlson and Herrick*'s [1990] relationship for oceanic crust for the crust of both upper and subducting plates. For the mantle wedge we assumed a constant vertical velocity gradient below the crust-mantle boundary and three different velocity-density conversion relationships: (1) *Carlson and Miller*'s [2003] relation for serpentinized peridotite; (2) *Birch*'s [1961] law for plagioclase, and diabase-gabbro-eclogite of oceanic layer 3; and (3) a constant density of 3200 kg/m^3 that is characteristic of unaltered uppermost mantle rocks. In all cases density and velocity were corrected from *in situ* to laboratory conditions and vice versa using experimental estimates of pressure (P) and temperature (T) partial derivatives for oceanic crust [*Korenaga et al*., 2001] and for serpentinized peridotite [*Kern and Tubia*, 1993].

[43] Figure 10a shows that the velocity-derived density model underestimates the gravity anomaly under the slope, where seismic velocity supports that fracturing is important (Figure 10d). However, a by 15% velocity increase in this area (green line) matches well the anomaly, whereas a velocity increased of 25% overestimates the gravity anomaly (blue line). This result means that the upper-plate *P* wave velocity that best predicts rock density is that corresponding to near-vertical propagation (Figure 6c), which is the least affected by the fractures causing seismic anisotropy in this area. This observation suggests that the elastic properties such as *P* wave velocity are more sensitive to rock fracturing than volumetric properties such as bulk density. This result supports the interpretation that the TWT mismatch between the two reflections is caused by velocity anisotropy, associated to a subvertical fracture system [*Carcione et al*., 2012].

[44] Tests on the density of the mantle wedge shows that serpentinized peridotite reproduces the observed gravity anomaly more accurately (green line in Figure 10b). Assuming that the $P_{mw}P$ reflection is not the Moho reflection, and converting velocity to density applying *Birch*'s [1961] law for oceanic layer 3 gabbros (red line), or using constant density of 3.2 g/cc of unaltered mantle rocks (blue line) overestimates the gravity anomaly, thus, gravity modeling supports a velocity-density conversion using a velocity increase of 15% with respect to the WAS velocity (Figure 4a) in the "fractured" area, and densities corresponding to serpentinized peridotite in the upper-plate "mantle wedge." The need for the presence of a

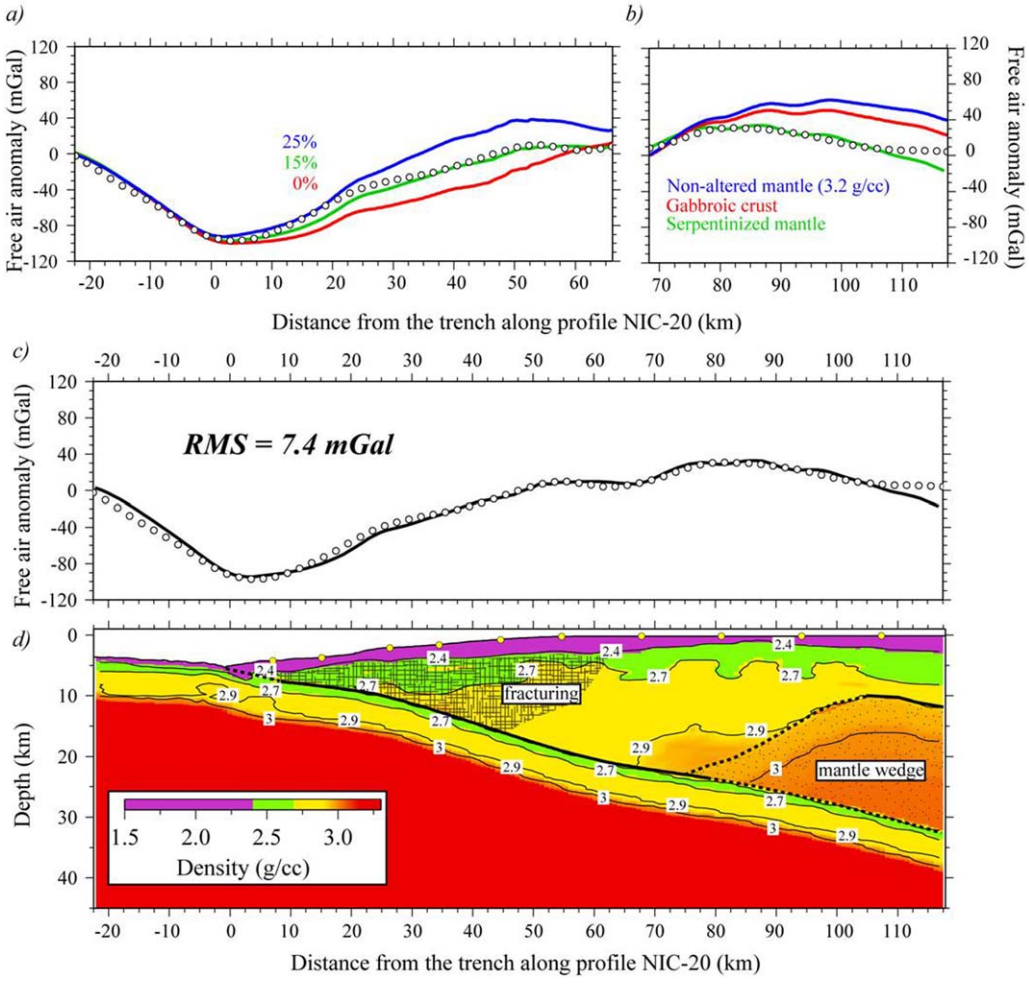

Figure 10. (a) Observed free-air gravity anomaly (white circles) and calculated gravity anomaly for three velocity-derived density models using *Hamilton et al.*'s [1978] relationship for shale for the sediment, *Carlson and Herrick*'s [1990] for oceanic crust for the overriding and subducting plates, and *Carlson and Miller*'s [2003] relationship for partially serpentinized peridotites in the zone labeled as "mantle wedge." The red line is obtained transforming the velocity model shown in Figure 4a, the green line increasing the velocity in the zone labeled as "fracturing" by 15% to account for seismic anisotropy (as in Figure 5c), and the blue line increasing the velocity in the same area by 25%. (b) Same as Figure 10a but in this case density in the "mantle wedge" is varied assuming a vertical velocity gradient of 0.03 s^{-1} below the crust-mantle boundary and velocity-density relationships corresponding to *Birch*'s [1961] law for plagioclase, and diabase-gabbro-eclogite of oceanic layer 3 (red line), *Carlson and Miller*'s [2003] relationship for partially serpentinized peridotites (green line), and a constant density of 3.2 g/cm^3 corresponding to nonaltered mantle (blue line). (c) Best gravity anomaly fit corresponding to the model obtained increasing the velocity in the zone labeled as "fracturing" by 15% and applying *Carlson and Miller*'s [2003] relationship for partially serpentinized peridotites in the "mantle wedge." (d) Density model corresponding to Figure 10c. Density units are g/cm^3.

shallow mantle wedge was also proposed based on gravity modeling along p80 profile [*Walther et al.*, 2000]. The density model including the subducting plate is shown in Figure 10d, with the "fractured" area extending to km ~60 from the trench axis, and the intersection of the inter-plate boundary and the tip of the "mantle wedge" at km ~80 from the trenchaxis. The gravity anomaly misfit for this model is 7.4 mGal (Figure 10c).

5.4. Multichannel Seismic Constraints on the Tectonic Structure and the Hydrogeological System

[45] The MCS images display structures that, together with the information on the nature and fracturing of the upper plate described above, help to interpret the dominant tectonic processes and hydrogeological system of the convergent margin.

The images show a deep ~8 km basin under the inner shelf underlain by a basement that does not show any evidence of significant faulting. The deep basin sediment is tilted and folded at several-kilometer-long wavelength in a manner described for the region in other profiles located to the north [*Ranero et al*., 2000], caused by early Miocene shortening. The deep sediment basin is separated by a ~20 km wide regional basement high from the outer shelf and slope sediment.

[46] The sediment overlying the flanks of the basement high show short-scale tilting indicating normal faulting with opposed vergence on either side of the high (Figure 5a). The outer shelf strata and top of the basement reflection are offset and tilted in numerous places indicating important landward-dipping normal faulting activity. The faults change dip polarity across the shelf edge and faulting dips seaward across the upper-middle slope. This abrupt change in fault dip polarity is accompanied by an increase in fault heave. Fault heave is difficult to calculate due to a fairly monotonous slope strata but the top of the basement reflection displays abrupt offsets of up to ~0.5 s TWT (roughly 0.5 km). Fault offsets at the seafloor are much smaller, which may indicate that they are growth faults, although mass-wasting processes have clearly truncated strata at the seafloor (Figure 5a).

[47] We interpreted that upper-plate extension by normal faulting is a response to tectonic erosion along the underside of the overriding plate as it has been observed elsewhere [*Ranero and von Huene*, 2000; *Ranero et al*., 2006]. The seaward dipping dominant fabric of the normal faults is probably a gravitational response of the overriding plate to a low-coupling environment along the plate boundary. The plate boundary is characterized under the slope and outer shelf by high-amplitude reflections that have been shown regionally to be commonly of reverse polarity, and that are indicative of the presence of abundant fluid at the fault zone [*Ranero et al*., 2008]. Open fractures along the plate boundary with fluids, as indicated by the lateral continuity of the plate boundary reflections in the dip and strike MCS lines, possibly require regionally widespread high pore pressures.

[48] Faulting across the slope of the region has been described from multibeam bathymetry maps and deep-towed side scan sonar data [*Ranero et al*., 2008; *Sahling et al*., 2008] and has been linked to seepage of deep sourced fluids arising from the dehydration of clays along the plate boundary [*Hensen et al*., 2004]. The model proposes that deep reaching normal faults provide fluid-flow paths for the water to raise from the plate boundary to the seafloor [*Ranero et al*., 2008]. The 15% basement-velocity anisotropy between subhorizontal (WAS data) and near-vertical (MCS reflection data) ray paths (Figure 6c), indicates the presence along the entire region of subvertical open fractures, located dominantly under the middle slope that probably correspond with fluid-filled normal faults feeding the seafloor seepage sites. This is the region where focused seepage at the seafloor has been more commonly observed [*Sahling et al*., 2008].

[49] The lateral coherency of slope strata and top of the basement reflection abruptly degrades from the middle to the lower slope (CMP 8300-8000) where individual strata are difficult to discern. The basement-velocity anisotropy of the middle slope has not been detected under the lower slope. We interpret that the abrupt decrease in strata coherency and rapid thinning of the overriding plate indicate that the amount of deformation increases rapidly from the upper-middle to the lower slope, perhaps related to the subduction of the seamount imaged in the MCS data (Figure 5). Further, we interpret that the absence of velocity anisotropy under the lower slope supports that the increased deformation has destroyed any preferred fracture orientation.

[50] Thus, the tectonic structure inferred from the seismic images supports a model of increased upper-plate deformation toward the front of the margin that does not occur linearly but presents abrupt changes due to the effect of seamount subduction and tectonic erosion (Figure 11).

5.5. The Downdip Limit of the Inter-Plate Seismogenic Zone

[51] The downdip limit of the inter-plate seismogenic zone (DLSZ) plays an important role as it determines the landward extension of the coseismic rupture in megathrust earthquakes. Its location is controlled by the frictional properties at the fault gouge, which are in turn modulated by a combination of thermal, structural and compositional factors. Although it is not entirely clear, which rock type is related to this limit, laboratory measurements show that most crustal rocks with composition similar to subducted sediments display a critical temperature of around 325–350°C that marks the transition from velocity-weakening to

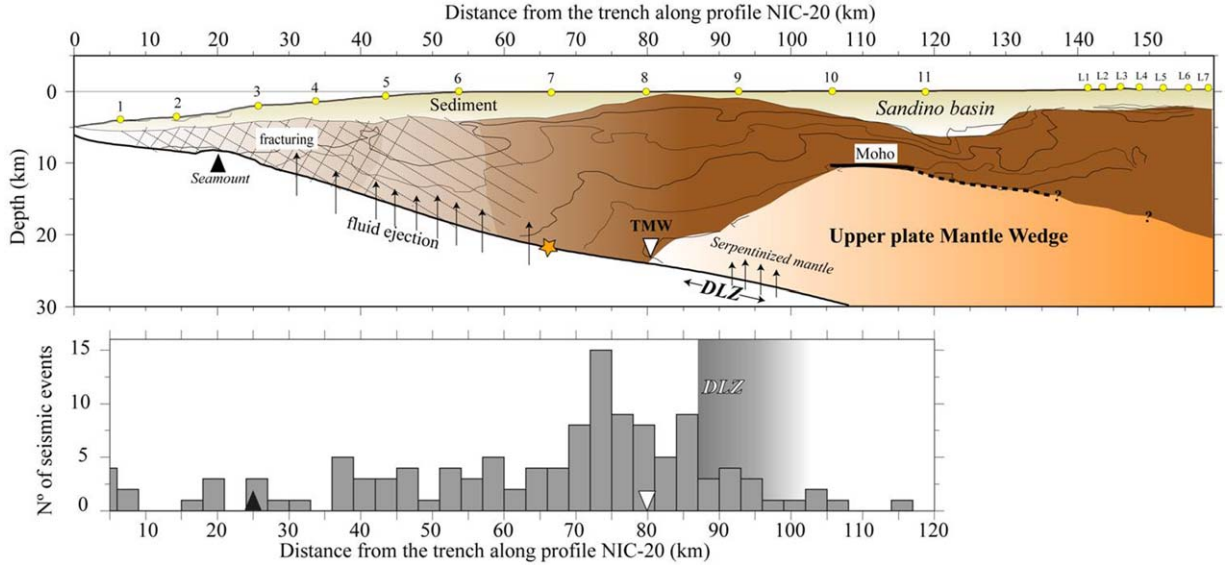

Figure 11. (a) Interpretative schematic cartoon of the tectonic structure and relationship to the seismogenic characteristics of the Nicaragua convergent margin. Orange star marks the projected hypocentral location of the 2 September 1992 tsunami earthquake. Abbreviations are EMW for Edge of the Mantle Wedge, and DLSZ for Downdip Limit of the Seismogenic Zone. (b) Histogram for the number of aftershocks of the 1992 earthquake as a function of the distance from the trench. Counts for 3 km wide boxes starting at the trench were computed. Aftershocks were projected to profile NIC-20. The epicentral locations corresponding to these events are shown in Figure 1b.

velocity-strengthening behavior [e.g., *Tse and Rice*, 1986; *Blanpied et al*., 1995]. These models were originally conceived for continental faulting, but they are also applied to oceanic subduction zones, so the 350–450°C isotherms have been commonly taken as a proxy to define the DLSZ [*Tichelaar and Ruff*, 1993; *Oleskevich et al*., 1999]. In warm subduction zones, such as Cascadia or SW Japan, the DLSZ is shallow (10–20 km). Its location coincides with that of the 350–450°C isotherms, so in these cases the DLSZ is believed to be thermally controlled [*Hyndman and Wang*, 1993; *Hyndman et al*., 1997]. However, in other cases, particularly in colder subduction zones such as Chile or Alaska, the DLSZ appears to coincide with the location of the upper-plate Moho, and not with the inferred location of the 350–450°C isotherms [e.g., *Oleskevich et al*., 1999]. This observation is surprising if we consider that dry mantle rocks are stronger than crustal compositions so faults cutting these rocks should in principle be seismogenic and display a velocity-weakening behavior at temperatures of up to 700–800°C [e.g., *Kirby*, 1983]. A proposed explanation for this limit is the hydration of the mantle wedge rocks by fluids expelled from the subducting slab [*Hyndman et al*., 1997; *Peacock and Hyndman*, 1999; *Schmidt and Poli*, 1998], transforming mantle peridotite into hydrated rocks such as serpentine and brucite. When present at the fault interface, the corresponding hydrous minerals exhibit a velocity-strengthening frictional behavior at the temperatures characteristic of the mantle wedge [e.g., *Peacock*, 1990; *Peacock and Hyndman*, 1999].

[52] *P* wave seismic velocity is sensitive to the presence of serpentinite, and laboratory experiments show that velocity decreases linearly by as much as 3.0–3.5 km/s between unaltered and 100% serpentinized peridotite for both high-T (containing antigorite) and low-T (containing lizardite and/or chrysotile) types [e.g., *Christensen*, 1966; *Watanabe et al*., 2007]. This is the reason why α is often taken as a proxy for the degree of mantle serpentinization, and it has been a primary evidence to propose mantle wedge serpentinization in numerous margins, including the MAT [e.g., *Walther et al*., 2000; *DeShon et al*., 2006]. In Nicaragua, a local earthquake tomography model with data recorded at an onshore-offshore seismic network displays a low velocity anomaly interpret as serpentinized mantle wedge centered beneath Sandino basin along the entire margin [*Dinc et al*., 2011]. Our seismic and gravity analysis results are consistent with this interpretation, and indicate that the mantle wedge is

at ~10 km depth under the shelf, and extends trenchward up to ~80 km from the trench (Figures 10 and 11).

[53] The number of aftershocks of the 1992 earthquake sharply decays landward from the inferred edge of the mantle wedge (Figure 11b). This location marks a limit in regional seismicity between a seismically active area updip, and a less active area downdip (Figure 1b). A seismic gap that appears to follow the whole Sandino basin, was first noted by *McIntosh et al*. [2007], although they suggested that it could be an artifact due to the poor azimuthal coverage of the offshore earthquakes recorded only onshore combined with the velocity model used for event location. Nonetheless, the new results from *Dinc et al*. [2011] show a similar distribution of seismic events with a gap beneath Sandino basin, evidencing that it is a robust feature rather than an artifact. We propose that the gap could be due to the presence of serpentinite minerals (e.g., antigorite) at the fault gouge, so that inter-plate fault dynamics under the mantle wedge would be dominated by stable sliding along the fault interface. Thus, the integration of aftershock distribution, the velocity structure, and density models (Figure 11), indicate that the gradual transition from unstable to stable sliding that defines the DLSZ would occur at around 90–100 km from the trench, near the edge of the mantle wedge (Figure 11).

5.6. The Updip Limit of the Inter-Plate Seismogenic Zone and Tsunamigenic Character of the 1992 Earthquake

[54] The 2 September 1992 Nicaragua earthquake is often cited as a textbook example of tsunami earthquake because it was the first one to be recorded by broadband seismic networks so that many details such as the energy released, the dimensions of the rupture area and the distribution of coseismic slip are very well documented [e.g., *Kikuchi and Kanamori*, 1995; *Satake*, 1995; *Ihmlé*, 1996a, 1996b]. This event excited a tsunami that was much larger than expected for its surface wave magnitude ($M_s = 7.2$). The aftershock activity was monitored for a period of 3 months after the main earthquake, resulting in a data set of 124 events with true moment magnitudes comprised between $M_w = 4.2$ and 5.5 (Figure 1b). According to the available locations, the aftershocks of this event are distributed almost up to the trench. The duration of the rupture was anomalously long (>100 s), as a consequence of an abnormally low rupture propagation velocity. Additionally, it is commonly accepted that the tsunamigenic character implies that the rupture of tsunami earthquakes must extend into the weak sediments of the accretionary wedge or the subduction channel [*Kanamori*, 1972; *Fukao*, 1979; *Okal*, 1988; *Pelayo and Wiens*, 1992; *Polet and Kanamori*, 2000].

[55] Seismological data inversion indicates that the source moment distribution of the 1992 earthquake was heterogeneous, showing patches with large slip (3–4 m) in the NW and SE limits of the rupture area within wider regions of modest or no slip, and a rupture propagation velocity varying from ~1.0 to 2.5 km/s [*Ihmlé*, 1996b]. A large proportion of the seismic moment was released close to the trench, as required to generate the tsunami [*Satake*, 1995; *Ihmlé*, 1996b]. This heterogeneous slip distribution is consistent with inversions of tsunami run-up data suggesting that a significant part of the energy was released near the SE limit [*Piatanesi et al*., 1996; *Geist and Bilek*, 2001]. To explain the characteristics of this earthquake, it has been proposed that it nucleated at <10 km deep [*Bilek and Lay*, 2002], most probably within the subducted sediments [*Kanamori and Kikuchi*, 1993; *Satake*; 1994]. Alternatively, *McIntosh et al*. [2007] noted that the area of maximum coseismic slip and slowest propagation velocity inferred from statistical analysis of seismological data [*Ihmlé*, 1996b] spatially coincides with subducted seamounts identified in the MCS data (Figure 1b). The spatial correspondence is particularly evident between the location of a large slip patch near the SE limit of the rupture area [*Ihmlé*, 1996b], the zone of larger tsunami energy release [*Piatanesi et al*., 1996; *Geist and Bilek*, 2001], and the seamount subducting beneath the lower-middle slope at 20–25 km from the trench that is imaged in MCS profiles NIC-28 [*McIntosh et al*., 2007] and NIC-20 (Figure 5a). This spatial coincidence led the authors to suggest a causal relationship between the SE subevent defined by the large slip patch, which occurred ~70 s after the main shock [*Ihmlé*, 1996b], and the presence of the subducted seamount.

[56] Accrding to *Scholz and Small* [1997], a situation that could favor the occurrence of unstable sliding spots is the presence of significant topographic relief on top of the subducting plate. Subducted seamounts and tall horsts locally alter the state of stress at the plate interface by increasing normal stress and hence seismic coupling. Thus, subduction of horsts and seamounts has been

proposed as an alternative mechanism to account for the occurrence of tsunami earthquakes near the trench [*Tanioka et al*., 1997; *Polet and Kanamori*, 2000]. Conversely, *Wang and Bilek* [2011] argue that subducted seamounts produce complex fracture networks during subduction that tend to produce numerous small earthquakes rather a single large event. Recent numerical work combining the effects of sliding along a fictional contact and the geometrical effects due to the presence of a seamount suggest that both factors play their role and the subducted seamounts can act both as barriers or asperities depending on different aspects such as the distance to the trench [*Yang et al*., 2012, 2013].

[57] In Nicaragua, the frontal 35–40 km of the inter-plate boundary (Figure 11), contains scattered but significant aftershock seismicity, indicating that the moderately fractured upper plate is able to store some elastic energy close to the trench axis and perhaps some amount of coupling along the interface. The nucleation of main shock of the 1992 event occurred at 65–70 km from the trench axis [*Ihmlé*, 1996a] and the seismic data indicates that initiated at 20–22 km deep. Subsequently, rupture propagated to the NW and SE and toward the trench [*Satake*, 1994; *Ihmlé*, 1996a, 1996b]. The distribution of coseismic slip within the rupture area was heterogeneous, with minor coseismic slip in most of the rupture area and small areas with large coseismic slip (Figure 1b). Our interpretation is that the propagation of the main shock triggered secondary events in some specific area of locally increased normal stress that became asperities. Such location of increased normal stress and measured larger slip is the subducting seamount near the SE limit of the rupture zone. We hypothesize that coseismic rupture of this seamount or other comparable areas with increased the normal stress close to the trench, in relatively low rigidity material [e.g., *Geist and Bilek*, 2001], is a key factor to explain the seafloor deformation and, therefore, the tsunamigenic character of this moderate-magnitude earthquake.

6. Conclusions

[58] The integration of WAS and gravity data modeling and coincident MCS images along a strike and dip transects acquired in the erosional convergent margin of Nicaragua provide constraints on the tectonic and seismic structure and physical properties of the overriding plate and the geometry of the inter-plate boundary.

[59] The velocity model shows vertical and lateral velocity gradients that are interpreted to reflect variations in the degree of fracturing and alteration of the basement igneous rock from a high disaggregation at the margin front to unaltered rocks at ~80 km from the trench axis. A general trenchward increase in fracturing inferred from WAS velocities agrees with the intensification of deformation from the upper-middle to the lower slope observed in the MCS images, probably enhanced by seamount subduction such as that imaged at 20–25 km from the trench.

[60] A systematic mismatch in travel time between the WAS and MCS inter-plate boundary reflections, is observed under the middle-upper slope. The mismatch is best explained by a velocity anisotropy of ~15% within the basement. Gravity analysis of velocity-derived density models supports this interpretation. The anisotropy can be explain by a local subvertical fracture network across the upper plate that may permit upward fluid migration, and that is located below the segment of the slope where seafloor seepage of deep-source fluids has been detected by previous studies.

[61] Under the continental shelf, upper mantle-like velocities are obtained beneath the Sandino forearc basin at a depth of ~10 km. The complementary gravity analysis supports the presence of a shallow, partially serpentinized upper-plate mantle wedge, with the crust-mantle transition intersecting the plate interface at ~80 km from the trench axis. The spatial coincidence between the location of the edge of the serpentinized mantle wedge and the deepest aftershocks of the 1992 event suggests that the transition from unstable to stable sliding that defines the downdip limit of the inter-plate seismogenic zone might be related to the presence of velocity-strengthening serpentine group minerals at the fault gouge.

[62] The subducting seamount imaged 20–25 km from the trench axis could have acted as a seismological asperity during the 1992 earthquake. This could explain the local patch of large coseismic slip and subsequent seafloor deformation needed to account for the seismological observations and tsunami runup data. The presence of this, and other, near-trench subducting seamounts might be key to explain the tsunamigenic character of the moderate-magnitude 1992 event.

Acknowledgments

[63] The seismic data presented in this work were collected during R/V Maurice Ewing cruise EW00–05 funded by NSF and German Science Foundation (DFG). A.M. has been supported by Kaleidoscope project financed by Repsol, and M.P. by the FPI programme of the Spanish Ministry of Science and Innovation (MICINN). Part of the work has been done in the framework of the MICINN-funded projects MEDOC (CTM2007–66179-C02-01/MAR and CTM2007–66179-C02-02/MAR) and HADES (CTM2011–30400-C02-01 and CTM2011–30400-C02-02). Most of the figures were generated with Generic Mapping Tools (GMT) software from *Wessel and Smith* [1998]. We thank Editor Thorsten Becker, reviewer Kelin Wang, and an anonymous reviewer, for their constructive reviews that helped improve the content of the manuscript.

References

Bangs, N., et al. (2004), Evolution of the Nankai Trough décollement from the trench into the seismogenic zone: Inferences from three-dimensional seismic reflection imaging, *Geology*, *32*, 273–276, doi:10.1130/G20211.1.

Baptista, A., G. Priest, and T. Murty (1993), Field survey of the 1992 Nicaragua tsunami, *Mar. Geod.*, *16*, 169–203.

Barkhausen, U., C. R. Ranero, R. von Huene, S. C. Cande, and H. A. Roeser (2001), Revised tectonic boundaries in the Cocos plate off Costa Rica: Implications for the segmentation of the convergent margin and for plate tectonic models, *J. Geophys. Res.*, *106*, 19,207–19,220.

Berhorst, A. (2006), Die Struktur des aktiven Kontinentalhangs vor Nicaragua und Costa Rica—Marin-seismische Steil- und Weitwinkelmessungen, PhD thesis, Christian-Albrechts-Univ., Kiel.

Bilek, S. L. and T. Lay (2002), Tsunami earthquakes possibly widespread manifestations of frictional conditional stability. *Geophys. Res. Lett.*. *29*, 1673, doi: 10.1029/2002GL015215.

Birch, F. (1961), The velocity of compressional waves in rocks to 10 kilobars, part 2, *J. Geophys. Res.*, *66*, 2199–2224.

Blanpied, M. L., D. A. Lockner, and J. D. Byeflee (1995), Frictional slip of granite at hydrothermal conditions, *J. Geophys. Res.*, *100*, 13,045–13,064.

Bourgois, J., J. Azema, P. O. Baumgartner, J. Tournon, A. Desmet, and J. Auboin (1984), The geologic history of the Caribbean-Cocos Plate boundary with special reference to the Nicoya ophiolite complex (Costa Rica) and D.S.D.P. results (Legs 67 and 84 off Guatemala): A synthesis. *Tectonophysics*. *108*, 1–32.

Carcione, J. M., S. Picotti, and J. E. Santos (2012), Numerical experiments of fracture-induced velocity and attenuation anisotropy, *Geophys. J. Int.*, *191*, 1179–1191, doi:10.1111/j.1365-246X.2012.05697.x.

Carlson, R. L., and C. N. Herrick (1990), Densities and porosities in the oceanic crust and their variations with depth and age, *J. Geophys. Res.*, *95*, 9153–9170.

Carlson, R. L., and D. J. Miller (2003), Mantle wedge water contents estimated from seismic velocities in partially serpentinized peridotites, *Geophys. Res. Lett.*, *30* (5), 1250, doi:10.1029/2002GL016600.

Christensen, N. I. (1966), Elasticity of ultrabasic rocks, *J. Geophys. Res.*, *71*, 5921–5931.

Christeson, G. L., K. D. McIntosh, T. H. Shipley, E. R. Flueh, and H. Goedde (1999), Structure of the Costa Rica convergent margin, offshore Nicoya Peninsula, *J. Geophys. Res.*, *104*, 25,443–25,468.

Crowe, J. C., and R. T. Buffler (1985), Multichannel seismic records across the Middle America Trench and Costa Rica-Nicaragua convergent margin, NCY-7 and NIC-1, in *Middle America Trench off Western Central America, Data Syn. Ser., Atlas 7*, edited by J. W. Ladd and R. T. Buffler, 11 pp., Ocean Margin Drill. Prog., Woods Hole, Mass.

DeMets, C., R. G. Gordon, D. F. Argus, and S. Stein (1994), Effect of recent revisions to the geomagnetic reversal timescale, *Geophys. Res. Lett.*, *21*, 2191–2194.

DeShon, H. R., S. Y. Schwartz, A. V. Newman, V. González, M. Protti, L. M. Dorman, T. H. Dixon, D. E. Sampson, and E. R. Flueh (2006), Seismogenic zone structure beneath the Nicoya Peninsula, Costa Rica, from three-dimensional local earthquake P- and S-wave tomography, *Geophys. J. Int.*, *164*, 109–124.

Dinc, A. N., W. Rabbel, E. R. Flueh, and W. Taylor (2011), Mantle wedge hydration in Nicaragua from local earthquake tomography, *Geophys. J. Int.*, *186*, 99–112, doi:10.1111/j.1365-246X.2011.05041.x.

Fisher, R. L. (1961), Middle America Trench: Topography and structure, *Geol. Soc. Am. Bull.*, *72*, 703–720.

Fukao, Y. (1979), Tsunami earthquakes and subduction processes near deep-sea trenches, *J. Geophys. Res. 84*, 2303–2314.

Gailler, A., P. Charvis, and E. R. Flueh (2007), Segmentation of the Nazca and South American plates along the Ecuador subduction zone from wide-angle seismic profiles, *Earth Planet. Sci. Lett.*, *260*, 444–464, doi:10.1016/j.epsl.2007.05.045.

Geist, E. L., and S. L. Bilek (2001), Effect of depth-dependent shear modulus on tsunami generation along subduction zones, *Geophys. Res. Lett.*, *28*, 1315–1318.

Hamilton, E. L. (1978), Sound velocity-density relations in sea-floor sediments and rocks, *J. Acoust. Soc. Am.*, *63*(2), 366–377.

Hensen, C., K. Wallmann, M. Schmidt, C. R. Ranero, and E. Suess (2004), Fluid expulsion related to mud extrusion off Costa Rica—A window to the subducting slab, *Geology*, *32*, 201–204.

Hinz, K., R. von Huene, C. R. Ranero, and Pacomar Working Group (1996), Tectonic structure of converging Pacific margin offshore Costa Rica from multichannel reflection seismic data SO 81, *Tectonics*, *15*, 54–66.

Hyndman, R. D., and S. M. Peacock (2003), Serpentinization of the forearc mantle, *Earth Planet. Sci. Lett.*, *212*, 417–432, doi:10.1016/S0012–821X(03)00263-2.

Hyndman, R. D., and K. Wang (1993), Thermal constraints on the zone of major thrust earthquake failure—The cascadia subduction zone, *J. Geopyhs. Res.*, *98*, 2039–2060.

Hyndman, R. D., M. Yamano, and D. A. Oleskevich (1997), The seismogenic zone of subduction thrust faults, *Island Arc*, *6*, 244–260.

Ihmlé, P. F. (1996a), Frequency-dependent relocation of the 1992 Nicaragua slow earthquake: An empirical Green's function approach, *Geophys. J. Int.*, *127*, 75–85.

Ihmlé, P. F. (1996b), Monte Carlo slip inversion in the frequency domain: Application to the 1992 Nicaragua slow earthquake, *Geophys. Res. Lett.*, *23*, 913–916.

Ivandic, M., I. Grevemeyer, A. Berhorst, E. R. Flueh, and K. D. McIntosh (2008), Impact of the bending-related faulting on the seismic properties of the incoming oceanic plate

offshore of Nicaragua, *J. Geophys. Res.*, *113*, B05410, doi:10.1029/2007JB005291.

Kanamori, H. (1972), Mechanism of tsunami earthquakes, *Phys. Earth Planet. Int.*, *6*, 346–359.

Kanamori, H., and M. Kikuchi (1993), The 1992 Nicaragua Earthquake: A slow tsunami earthquake associated with subducted sediments, *Nature*, *361*, 714–716.

Kern, H., and J. M. Tubia (1993), Pressure and temperature dependence of P- and S-wave velocities, seismic anisotropy and density of sheared rocks from the sierra alpujata massif (ronda peridotites, southern Spain), *Earth Planet. Sci. Lett.*, *119*(1-2), 191–205.

Kikuchi, M., and H. Kanamori (1995), The Shikotan earthquake of October 4, 1994: Lithospheric earthquake, *Geophys. Res. Lett.*, *22*, 1025–1028.

Kimura, G., E. Silver, P. Blum, and Shipboard Scientific Party (1997), Proceedings of the Ocean drilling Program, Initial Rep. 170, Ocean Drill. Program, College Station, Tex.

Kirby, S. H. (1983), Rheology of the lithosphere, *Rev. Geophys. Space Phys.*, *21*, 1458–1487.

Korenaga, J., W. S. Holbrook, G. M. Kent, P. B. Kelemen, R. S. Detrick, H. -C. Larsen, J. R. Hopper, and T. Dahl-Jensen (2000), Crustal structure of the southeast Greenland margin from joint refraction and reflection seismic tomography, *J. Geophys. Res.*, *105*, 21,591–21,614.

Korenaga, J., W. S. Holbrook, R. S. Detrick, and P. B. Kelemen (2001), Gravity anomalies and crustal structure at the southeast Greenland margin, *J. Geophys. Res.*, *106*, 8853–8870.

Kronenberg, A., and G. L. Shelton (1980), Deformation microstructures in experimentally deformed Maryland diabase, *J. Struct. Geol.*, *2*(3), 341–353.

Lefeldt, M., C. R. Ranero, and I. Grevemeyer (2012), Seismic evidence of tectonic control on the depth of water influx into incoming oceanic plates at subduction trenches, *Geochem. Geophys. Geosyst.*, *13*, Q05013, doi:10.1029/2012GC004043.

Marone, C., and D. M. Saffer (2007), Fault friction and the upper transition from seismic to aseismic faulting, in *The Seismogenic Zone of Subduction Thrust Faults*, edited by T. Dixon et al., pp. 346–369, Columbia Univ. Press., New York.

McIntosh, K. D., E. Silver, and T. Shipley (1993), Evidence and mechanisms for forearc extension at the accretionary Costa Rica convergent margin, *Tectonics*, *12*, 1380–1392.

McIntosh, K. D., E. A. Silver, I. Ahmed, A. Berhorst, C. R. Ranero, R. K. Kelly, and E. R. Flueh (2007), The Nicaragua convergent margin, in *The Seismogenic Zone of Subduction Thrust Faults, Part III*, edited by T. H. Dixon and J. C. Moore, chap. 9, pp. 257–287, Columbia Univ. Press, New York.

Moore, J. C., and D. Saffer (2001), Updip limit of the seismogenic zone beneath the accretionary prism of Southwest Japan: An effect of diagenetic to lowgrade metamorphic processes and increasing effective stress, *Geology*, *29*(2), 183–186.

Moore, J. C., and P. Vrolijk (1992), Fluids in accretionary prisms, *Rev. Geophys.*, *30*, 113–135.

Mukerji, T., J. Berryman, G. Mavko, and P. Berge (1995), Differential effective medium modelling of rock elastic moduli with critical porosity constraints, *Geophys. Res. Lett.*, *22*, 555–558.

Nur, A., G. Mavko, J. Dvorkin, and D. Galmudi (1998), Critical porosity: A key relating physical properties to porosity in rocks, *Leading Edge*, *17*, 357–362.

Okal, E. A. (1988), Seismic parameters controlling far-field tsunami amplitudes: A review, *Nat. Hazards*, *1*, 67–96.

Oleskevich, D. A., R. D. Hyndman, and K. Wang, (1999), The updip and downdip limits to great subduction earthquakes: Thermal and structural models of Cascadia, South Alaska, SW Japan, and Chile, *J. Geophys. Res.*, *104*, 14,965–14,992.

Pacheco, J., L. R. Sykes, and C. H. Scholz (1993), Nature of seismic coupling along simple plate boundaries of the subductton plate, *J. Geophys. Res.*, *98*, 14,133–14,159.

Paige, C. C., and M. A. Saunders (1982), LSQR: An algorithm for sparse linear equations and sparse least squares, *Trans. Math. Software*, *8*, 43–71.

Papazachos, C., and G. Nolet (1997), P and S deep velocity structure of the Hellenic area obtained by robust nonlinear inversion of travel-times, *J. Geophys. Res.*, *102*, 8349–8367.

Parker, R. L. (1974), New method for modelling marine gravity and magnetic anomalies, *J. Geophys. Res.*, *79*, 2014–2016.

Peacock, S. M. (1990), Fluid processes in subduction zones, *Science*, *48*, 329–337.

Peacock, S. M., and R. D. Hyndman (1999), Hydrous minerals in the mantle wedge and the maximum depth of subduction thrust earthquakes, *Geophys. Res. Lett.*, *26*, 2517–2520, doi:10.1029/1999GL900558.

Pelayo, A. M., and D. A. Wiens (1992), Tsunami earthquakes; slow thrust-faulting events in the accreationary wedge, *J. Geophys. Res.*, *97*, 15,321–15,337.

Piatanesi, A., S. Tinti, and I. Gavagni (1996), The slip distribution of the 1992 Nicaragua earthquake from tsunami run-up data, *Geophys. Res. Lett.*, *23*, 37–40.

Polet, J., and H. Kanamori (2000), Shallow subduction zone earthquakes and their tsunamigenic potential, *Geophys. J. Int.*, *142*, 684–702.

Ranero, C. R., and R. von Huene, (2000), Subduction erosion along the Middle America convergent margin, *Nature*, *404*, 748–755, doi:10.1038/35008046.

Ranero, C. R., R. von Huene, E. R. Flueh, M. Duarte, D. Baca, and K. D. McIntosh (2000), A cross section of the convergent Pacific margin of Nicaragua, *Tectonics*, *19*, 335–357.

Ranero, C. R., R. von Huene, W. Weinrebe, and C. Reichert (2006), Tectonic processes along the Chile convergent margin, in *The Andes—Active Subduction Orogeny. Frontiers in Earth Sci.*, vol. *1*, XXII, edited by O. Oncken et al., pp. 91–121, Springer, Berlin, Heidelberg.

Ranero, C. R., R. von Huene, W. Weinrebe, and U. Barckhausen (2007), Convergent margin tectonics of Middle America: A marine perspective, in *Central America, Geology, Hazards and Resources*, edited by G. Alvarado and J. Bunschu, pp. 239–265, A.A. Balkema, Leiden, The Netherlands.

Ranero, C. R., I. Grevemeyer, H. Sahling, U. Barckhausen, C. Hensen, K. Wallmann, W. Weinrebe, P. Vannucchi, R. von Huene, and K. McIntosh (2008), The hydrogeological system of erosional convergent margins and its influence on tectonics and interplate seismogenesis, *Geochem. Geophys. Geosyst.*, *9*, Q03S04, doi:10.1029/2007GC001679.

Ruff, L. J., and H. Kanamori (1983), Seismic coupling and uncoupling at subduction zones, *Tectonophysics*, *99*, 99–117.

Sahling, H., D. G. Masson, C. R. Ranero, V. Hühnerbach, W. Weinrebe, I. Klaucke, D. Bürk, W. Brückmann, and E. Suess (2008), Fluid seepage at the continental margin offshore Costa Rica and southern Nicaragua, *Geochem. Geophys. Geosyst.*, *9*, Q05S05, doi:10.1029/2008GC001978.

Sallarès, V., and C. R. Ranero (2005), Structure and tectonics of the erosional convergent margin off Antofagasta, north

Chile (23°30′S), *J. Geophys. Res.*, *110*, B0601, doi:10.1029/2004JB003418.

Sallarès, V., J. J. Danobeitia, E. R. Flueh, and G. Leandro (1999), Seismic velocity structure across the Middle American landbridge in northern Costa Rica, *J. Geodyn.*, *27*, 327–344.

Sallarès, V., J. J. Dañobeitia, and E. R. Flueh (2000), Seismic tomography with local earthquakes in Costa Rica, *Tectonophysics*, *329*, 61–79.

Sallarès, V., P. Charvis, E. R. Flueh, and J. Bialas (2003), Seismic structure of Malpelo and Cocos Volcanic Ridges and implications for hotspot-ridge interaction, *J. Geophys. Res.*, *108*(B12), 2564, doi:10.1029/2003JB002431.

Sallarès, V., P. Charvis, E. R. Flueh, J. Bialas, and The SALIERI Scientific Party (2005), Seismic structure of the Carnegie ridge and nature of the Galápagos hotspot, *Geophys. J. Int.*, *165*, 763–788.

Sallarès, V., A. Gailler, M.-A. Gutscher, D. Graindorge, R. Bartolomé, E. Gràcia, J. Díaz, J. J. Dañobeitia, and N. Zitellini (2011), Seismic evidence for the presence of Jurassic oceanic crust in the central Gulf of Cadiz (SW Iberian margin), *Earth Planet. Sci. Lett.*, *311*(1-2), 112–123, doi:10.1016/j.epsl.2011.09.00.

Sallarès, V., S. Martínez-Loriente, M. Prada, E. Gràcia, C. R. Ranero, M.-A. Gutscher, R. Bartolomé, Gailler, J. J. Dañobeitia, and N. Zitellini (2013), Seismic evidence of exhumed mantle rock basement at the Gorringe Bank and the adjacent Horseshoe and Tagus abyssal plains (SW Iberia), *Earth Planet. Sci. Lett.*, *365*, 120–131, doi:10.1016/j.epsl.2013.01.021.

Sandwell, D. T., and W. H. F. Smith (2009), Global marine gravity from retracked Geosat and ERS-1 altimetry: Ridge segmentation versus spreading rate, *J. Geophys. Res.*, *114*, B01411, doi:10.1029/2008JB006008.

Satake, K. (1994), Mechanism of the 1992 Nicaragua tsunami earthquake, *Geophys. Res. Lett.*, *21*, 2519–2522.

Satake, K. (1995), Linear and nonlinear computations of the 1992 Nicaragua earthquake tsunami, *Pure Appl. Geophys.*, *144*, 455–470.

Satake, K., J. Bourgeois, K. Abe, Y. Tsuji, F. Imamura, Y. Iio, H. Katao, E. Noguera, and F. Estrada (1993), Tsunami field survey of the 1992 Nicaragua earthquake, *Eos Trans. AGU*, *74*, 145–156.

Schmidt, M. W., and S. Poli (1998), Experimentally based water budgets for dehydrating slabs and consequences for arc magma generation, *Earth Planet. Sci. Lett.*, *163*, 361–379.

Scholz, C. H. (1998), Earthquakes and friction laws, *Nature*, *391*, 37–42.

Scholz, C. H., and J. Campos (1995), On the mechanism of seismic decoupling and back arc spreading at subduction zones, *J. Geophys. Res.*, *100*, 22,103–22,115.

Scholz, C. H., and C. Small (1997), The effect of seamount subduction on seismic coupling, *Geology*, *25*(6), 487–490.

Seely, D. R., P. R. Vail, and G. G. Walton (1974), Trench slope model, in *Geology of Continental Margins*, edited by C. A. Burk and C. L. Drake, pp. 261–283, Springer, New York.

Silver, E., A. Fisher, D. Saffer, M. Kastner, J. Morris, and K. D. McIntosh (2000), Fluid flow paths in the middle America Trench and Costa Rica margin, *Geology*, *28*(8), 679–682, doi:10.1130/0091–7613.

Stavenhagen, A. U., E. R. Flueh, C. R. Ranero, K. D. McIntosh, T. Shipley, G. Leandro, A. Shulze, and J. J. Danobeitia (1998), Seismic wide-angle investigations in Costa Rica: A crustal velocity model from the Pacific to the Caribbean coast, *Zent. Geol. Paläontol.*, *3–6*, 393–408.

Stoffa, P. L., T. H. Shipley, D. Dean, W. Kessinger, E. Silver, D. Reed, and A. Aguilar (1991), Three dimensional seismic imaging of the Costa Rica accretionary prism: Field program and migration examples, *J. Geophys. Res.*, *96*, 21,693–21,721.

Tanioka, Y., L. Ruff, and K. Satake (1997), What controls the lateral variation of large earthquake occurrence along the Japan trench, *Island Arc*, *6*, 261–266.

Tarantola, A. (1987), *Inverse Problem Theory: Methods for Data Fitting and Model Parameter Estimation*, Elsevier Sci., New York.

Tichelaar, B. W., and L. J. Ruff (1993), Depth of seismic coupling along subduction zones, *J. Geophys. Res.*, *98*, 2017–2037.

Toomey, D. R., and G. R. Foulger (1989), Tomographic inversion of local earthquake data from the Hengill-Grensdalur central volcano complex, Iceland, *J. Geophys. Res.*, *94*, 17,497–17,510.

Toomey, D. R., S. C. Solomon, and G. M. Purdy (1994), Tomographic imaging of the shallow crustal structure of the East Pacific Rise at 9°30′N, *J. Geophys. Res.*, *99*, 24,135–24,157.

Tse, S. T., and J. R. Rice (1986), Crustal earthquakes instability relation to the depth variation of frictional slip properties, *J. Geophys. Res.*, *91*, 9452–9472.

Vannuchi, P., C. R. Ranero, S. Galeotti, S. M. Straub, D. W. Scholl, and K. McDougall-Ried (2003), Fast rates of subduction erosion along the Costa Rica Pacific margin: Implications for nonsteady rates of crustal recycling at subduction zones, *J. Geophys. Res.*, *108*(B11), 2511, doi:10.1029/2002JB002207.

Vannucchi, P., S. Galeotti, P. D. Clift, C. R. Ranero, and R. von Huene (2004), Long-term subduction-erosion along the Guatemalan margin of the Middle America Trench, *Geology*, *32*(7), 617–620, doi:10.1130/G20422.1.

van Avendonk, H. J. A., A. J. Harding, and J. A. Orcutt (1998), A two-dimensional tomographic study of the Clipperton transform fault, *J. Geophys. Res.*, *103*, 17,885–17,899.

von Huene, R., L. D. Kulm, and J. Miller, (1985), Structure of the frontal part of the Andean Convergent Margin, *J. Geophys. Res.*, *90*, 5429–5442.

von Huene, R., C. R. Ranero, W. Weinrebe, and K. Hinz (2000), Quaternary convergent margin tectonics of Costa Rica, segmentation of the Cocos Plate, and Central American volcanism, *Tectonics*, *19*, 314–334.

von Huene, R., C. R. Ranero, and P. Vannucchi (2004), A model for subduction erosion, *Geology*, *32*, 913–916, doi:10.1130/G20563.1.

Walther, C. H. E., E. R. Flueh, C. R. Ranero, R. von Huene, and W. Strauch (2000), Crustal structure across the Pacific margin of Nicaragua: Evidence for ophiolitic basement and a shallow mantle sliver, *Geophys. J. Int.*, *141*, 759–777.

Wang, K., and S. L. Bilek (2011), Do subducting seamounts generate or stop large earthquakes?, *Geology*, *39*, 819–822, doi:10.1130/G31856.1.

Ward, S. N. (1980), Relationship of tsunami generation and an earthquake source, *J. Phys. Earth*, *28*, 441–474.

Watanabe, T., H. Kasami, and S. Ohshima (2007), Compressional and shear wave velocities of serpentinized peridotites up to 200 MPa, *Earth Planets Space*, *59*(4), 233–244.

Wessel, P., and W. H. F. Smith (1998), New, improved version of the generic mapping tools released, *Eos Trans. AGU*, *79*, 579.

White, R. S., D. McKenzie, and R. K. O'Nions (1992), Oceanic crustal thickness from seismic measurements and Rare Earth Element inversions, *J. Geophys. Res.*, *97*, 19,683–19,715.

Yang, H., Y. Liu, and J. Lin (2012), Effects of subducted seamounts on megathrust earthquake nucleation and rupture propagation, *Geophys. Res. Lett.*, *39*, L24302, doi:10.1029/2012GL053892.

Yang, H., Y. Liu, and J. Lin (2013), Geometrical effects of a subducted seamount on stopping megathrust ruptures, *Geophys. Res. Lett.*, *40*, doi:10.1002/grl.50509.

Ye, S., J. Bialas, E. R. Flueh, A. Stavenhagen, and R. von Huene (1996), Crustal structure of the Middle American Trench off Costa Rica from wide-angle seismic data, *Tectonics*, *15*, 1006–1021.

Zelt, C. A., and R. B. Smith (1992), Seismic traveltime inversion for 2-D crustal velocity structure, *Geophys. J. Int.*, *108*, 16–34.